IMPLEMENTING FRET SPECTROMETRY USING TIME RESOLVED FLUORESCENCE MICROSCOPY FOR DETERMINATION OF PROTEIN OLIGOMER SIZE AND GEOMETRY IN LIVE CELLS

by

Aliyah Sephrah Khan

A Thesis Submitted in
Partial Fulfillment of the
Requirements for the Degree of

Master of Science
in Physics
at
The University of Wisconsin-Milwaukee
May 2024

ABSTRACT

IMPLEMENTING FRET SPECTROMETRY USING TIME RESOLVED FLUORESCENCE MICROSCOPY FOR DETERMINATION OF PROTEIN OLIGOMER SIZE AND GEOMETRY IN LIVE CELLS

by

Aliyah Sephrah Khan

The University of Wisconsin-Milwaukee, 2024

Under the Supervision of Professor Valerică Raicu

Förster or Fluorescence Resonance Energy Transfer (FRET) is a biological phenomenon that occurs when energy is transferred non-radiatively from an excited donor molecule to an unexcited acceptor molecule when they are a certain distance from each other. One method of conducting FRET experiments is using FRET spectrometry which was previously introduced by the Raicu Lab. This method generates histograms of FRET efficiencies at pixel level called FRET spectrograms, that are fitted with models to determine the quaternary structure of protein oligomers as opposed to traditional FRET experiments which average over all FRET efficiencies. Currently, FRET spectrometry is implemented with spectrally resolved fluorescence microscopy to allow the computation of FRET efficiencies where the size of the oligomer is unknown.

Another technique, Fluorescence Lifetime Imaging Microscopy (FLIM) has been successfully used to compute FRET efficiencies by fitting fluorescence decay curves with one or two exponential fits in order to determine the fluorescence lifetimes in the presence and absence of the donors and acceptors. However, using FLIM to study oligomers of arbitrary size is limited by the prerequisite knowledge of the distinct oligomeric configurations, as well as the mathematical limitation of extracting more than two lifetimes from a single decay. The tiFRET method was developed to address these limitations by numerically integrating the fluorescence decay curves at each pixel in order to determine the pixel level FRET efficiencies and generate FRET spectrograms. The tiFRET method was initially tested on cytoplasmic constructs of Cerulean, Venus, and Amber and compared to the traditional FLIM measurements using one and two lifetime fits. This method was then applied to a biological system that was known to oligomerize and compared to traditional FRET spectrometry experiments.

G protein coupled receptors (GPCRs) are the largest family of membrane proteins. These receptors mediate most cellular responses to external stimuli, making them ideal candidates for drug research and development. In this study, the human muscarinic acetylcholine receptor M_2 (M_2R), one of five human muscarinic acetylcholine receptors, a class A- rhodopsin like GPCR was used. M_2R is primarily responsible for slowing down the heart rate by controlling the rate of depolarization of the cell membrane by causing an outward flow of potassium ions. There are various studies that show the tendency of the muscarinic receptors to oligomerize, which was ideal for this study. Using two variants of the green fluorescent protein (GFP_2, green fluorescent protein and YFP, yellow fluorescent protein) as fluorescent markers, two-photon fluorescence microscopy was used to collect temporally resolved fluorescence images and spectrally resolved fluorescence images of live cells. The tiFRET method was applied to the temporally resolved fluorescence images to calculate the pixel level distributions of apparent FRET efficiencies and obtain FRET spectrograms. The spectrally resolved fluorescence images were analyzed using the currently established method of performing FRET spectrometry to obtain FRET spectrograms. FRET metahistograms were generated and fit with a theoretical model in order to determine the oligomeric configuration of M_2R. Both metahistograms were compared to determine the viability of the novel tiFRET method. In this study, the results of this comparison and future research are presented.

Dedicated to my family and loved ones.

This was only possible because of your unwavering love and support.

TABLE OF CONTENTS

LIST OF FIGURES viii
LIST OF TABLES x
LIST OF ABBREVIATIONS xii
ACKNOWLEDGEMENTS xiii
Chapter 1. Introduction **1**
1.1 Protein Structure 2
1.2 Cell Membrane and Membrane Proteins 7
1.2.1 Cell Membrane 7
1.2.2 Membrane Proteins 8
1.3 G Protein-Coupled Receptor (GPCRs) 10
1.3.1 Ligand and Ligand Binding 12
1.3.2 The Human Muscarinic Acetylcholine Receptors 13
1.4 Oligomerization 15
1.4.1 Oligomerization of G Protein-Coupled Receptors 16
Chapter 2. Fluorescence Based Detection Techniques 18
2.1 Fluorescent Proteins 18
2.2 Fluorescence-Based Detection of Proteins 19
2.3 Förster (or Fluorescence) Resonance Energy Transfer (FRET) 23
2.4 Fluorescence Lifetime Imaging Microscopy (FLIM) 27
2.5 Oligomerization and FRET 29
2.6 GPCR Oligomerization Studies 32
Chapter 3. Methods 37
3.1 Cell Culture and Cell Sample Preparation 37
3.2 Transfection 39
3.3 Time-resolved fluorescence imaging 40
3.4 Two-photon Fluorescence Microspectroscopy 44
3.5 Calculation of Apparent FRET Efficiency Using Temporal Resolution 46
3.6 Calculation of Apparent FRET Efficiency Using Spectral Resolution 51
3.7 Analysis of Metahistogram using Parallelogram Shaped Tetramer Model 53
Chapter 4. Results 58
4.1 Determining the Fluorescence Lifetime of the Donor 60

4.2 Obtaining E_{app} and F_D only maps for the Temporally Resolved Experiments 62
4.3 Obtaining E_{app} and F_D only maps for the Spectrally Resolved Experiments 64
4.4 Generating Metahistograms 65
4.5 Automatic Iterative Fitting Procedure 67
4.6 Metahistogram Fitting with Substates 68
Chapter 5. Discussion and Further Research.....74
References 79

LIST OF FIGURES

Figure 1.1 General structure of an amino acid……..3

Figure 1.2. Formation of a polypeptide chain……...4

Figure 1.3. Diagram of the primary structure of the protein……4

Figure 1.4. Diagram of the secondary structures of proteins...…….....5

Figure 1.5. Diagram of the tertiary structure of a protein……6

Figure 1.6. Diagram of the quaternary structure of a protein……7

Figure 1.7. Diagram of the cell membrane……8

Figure 1.8. Diagram showing the different types of membrane proteins……9

Figure 1.9. Diagram of a G protein-couple receptor……...11

Figure 1.10. Diagram of a GPCR bound to a ligand orthosterically……12

Figure 1.11. Diagram of the human muscarinic receptor M_2……14

Figure 1.12. Diagram of Collagen as a homo-oligomer……..15

Figure 2.1. Diagram of the green fluorescent protein……19

Figure 2.2. Schematic representation of fluorescence……20

Figure 2.3. Schematic of the energy transfer process between a donor and acceptor……25

Figure 2.4 Schematic showing the shortening of the donor lifetime due to FRET……29

Figure 2.5 Schematic showing the apparent FRET efficiencies for various configurations of donors and acceptors…….……31

Figure 3.1. Schematic of the setup of equipment used during transfection……40

Figure 3.2. Schematic of the typical experimental setup for the multiphoton microscope used in the temporally resolved experiments……..42

Figure 3.3 Schematic of OptiMiS Setup used in spectrally resolved experiments……..45

Figure 3.4 Illustration of the fluorescence decay curves from each pixel in the image with an exponential decay fit or integrated…….47

Figure 3.5 Experimental lifetime of the green fluorescent protein attached to M_2R……49

Figure 3.6 Generation of FRET and FD only maps…….50

Figure 3.7 Schematic of the parallelogram shaped tetramer used for the fitting model and the description of the geometric variables……54

Figure 3.8 Typical diagram depicting the automatic iterative fitting procedure of the geometric model applied to the FRET efficiency metahistograms……..56

Figure 4.1. Experimental lifetime of green fluorescent protein attached to the human muscarinic receptor 2……62

Figure 4.2. Illustration of the FRET efficiency distribution map and F_D only map……64

Figure 4.3. Four-dimensional representation of the iterative process of lowering the fitting residual……...68

Figure 4.4. Illustration of the fitted metahistogram for the human muscarinic receptor 2 with fluorescent proteins attached…….70

Figure 5.1. Schematic of a spectrum from an individual pixel with bandwidth filter overlayed…….77

LIST OF TABLES

Table 3.1 showing FRET efficiencies for each configuration for the parallelogram shaped tetramer model…….55

Table 4.1. Best-Fit Geometric Variables for the Tetrameric Model Used to Determine the Quaternary Structure of the Human Muscarinic Receptor, M_2R, Using Temporal and Spectral Resolution……...71

Table 4.2. Calculated Distances for the Parallelogram Shaped Oligomer for the Human Muscarinic Receptor, M_2R, Using Temporal and Spectral Resolution…….72

ACKNOWLEDGEMENTS

First and foremost, I am profoundly thankful to God for granting me the strength, wisdom, and perseverance to navigate through the challenges and obstacles encountered during the research process. His divine presence has been a source of comfort and inspiration, sustaining my spirit during moments of uncertainty and doubt.

I would like to acknowledge and express my gratitude to my advisor, Dr. Valerică Raicu, and my committee members, Dr. Sarah Vigeland and Dr. Ionel Popa, for their invaluable guidance and support throughout my thesis. This work would not have been possible without these individuals who have provided their perceptive and insightful expertise to better my understanding and augment the quality of my work.

In addition, I am extremely grateful to research scientist, Dr. Michael Stoneman, and members of Raicu Lab, Thomas Killeen, Justin Trujillo, and Dhruba Adhikari. The constructive and educated assistance of these members allowed for an instrumental progression of this study and aided in the overall management of challenges. Their feedback and support were indispensable in enhancing my determination and motivation and has made my experience more enjoyable.

Moreover, it would be remiss to not acknowledge members of LOCI at UW Madison, Dr. Kevin Eliceiri and Dr. Jenu Chacko. I am eternally appreciative that they have allowed us to use their facilities. This work and my findings would not be possible without them.

Lastly, I would like to extend a special thanks to my family and friends for their unwavering support and faith in me. Their understanding and prayers immensely helped me through ups and

downs and kept me going in the hardest of times. They were a source of strength and love, and their encouragement and advice were immeasurable to my experience throughout my research.

Chapter 1

INTRODUCTION

G-protein coupled receptors (GPCRs) are a type of integral membrane protein easily identified by their characteristic seven α-helical transmembrane domains [1]. GPCRs are the most common type of cell receptors with more than 800 distinct GPCRs and nearly 4% of the protein coding genome [2]. They have a wide array of physiological functions ranging from but not limited to their involvement in the senses such as visual, gustatory, and olfactory, mood regulation, their roles in the central and peripheral nervous system to regulating hormonal responses in the endocrine system. Due to this diversity in function, GPCRs are a major target for therapeutic drugs with approximately 30% of all identified drug targets being GPCRs [1]. This superfamily of proteins is subdivided into six classes/families: A-F, based on structural similarities [3]. The largest of these families is family A- rhodopsin like with approximately 90% of the GPCRs belonging to this family [1].

The human muscarinic acetylcholine receptors are a class A GPCR subdivide into five distinct categories depending on the function of the receptor ($M_{1\text{-}5}R$) that bind to the neurotransmitter, acetylcholine [4]. They are predominantly found in the parasympathetic nervous system (PNS) and has excitatory and inhibitory control over the organs and tissues with in the PNS, resulting in regulation of a number of physiological functions including heart rate, cognition, and motor control [4]. Drugs targeting the muscarinic receptors are used for treatments for a variety of conditions including: Alzheimer's disease, chronic obstructive pulmonary disease, and overactive bladder [5].

Muscarinic receptor M_2R is crucial to the parasympathetic nervous system specifically due to its role in cardiovascular function. By regulating the potassium channels, M_2R is responsible for slowing down the heart rate [6].

Traditionally, GPCRs were thought to operate as monomers when regulating physiological function, however there is growing evidence that GPCRs can actually self-associate and/or associate with other receptors in a process called oligomerization [7]. Oligomerization plays important roles in cell surface delivery, signaling and a variety of other functions. The muscarinic receptors have been known to dimerize (form pairs) as well as potentially higher oligomers [8].

The process of oligomerization is often studied using fluorescence imaging techniques with both temporal and spectral resolution. In this study, the applicability of a novel method to determine the quaternary structure of M_2R in live cells was explored. Using both temporal and spectral resolution, FRET (Förster resonance energy transfer) spectrometry experiments were conducted to determine the viability of the novel temporally resolved technique.

In this chapter, a general background for the research presented is established. Protein structures, G-protein coupled receptors, the target receptor M_2R, and the mechanisms of oligomerization are introduced.

1.1 Protein Structure

Proteins are a class of biomolecules that are made up of elementary building blocks called amino acids. The main parts of the amino acid comprise of the amine group (NH_2), the carboxyl group (COOH), one hydrogen atom, and the residue (R-group) as shown in figure 1.1. The unique R-group is used to differentiate between 20 amino acids [9]. The amino acids are further broken up

into four subgroups based on their side chains: electrically charged, polar, hydrophobic and special cases [10].

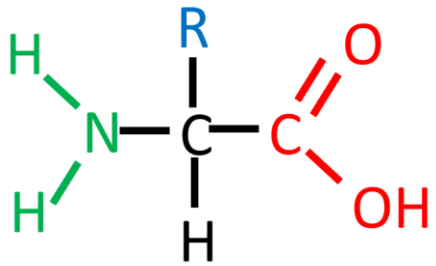

Figure 1.1. General structure of an amino acid. Amino acids contain an amine group (green) and a carboxyl group (red). The R group (blue) of the amino acid has a variety of unique structures that differentiate the various amino acids from one another and influence the interactions of amino acids with each other.

Polymers of amino acids form polypeptide chains when the amine and carboxyl group of the amino acids are covalently bound together resulting in the loss of a water molecule (see fig 1.2). Convention dictates that the free amine group or the N-terminus starts the polypeptide sequence, and the free carboxyl group or C-terminus ends the polypeptide chain

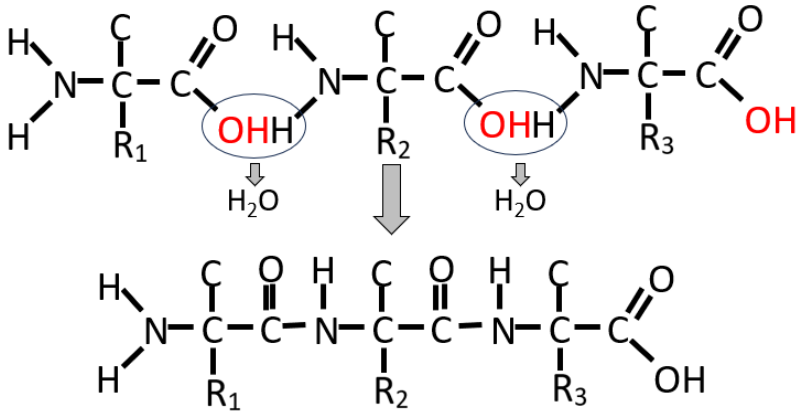

Figure 1.2. Formation of a polypeptide chain. The OH from the carboxylic group binds to the H from the amine group of the amino acid to form a water molecule, leaving the carbon and nitrogen atoms free to covalently bind to each other. This forms the polypeptide chain.

These polypeptide chains make up the primary structure of the protein (see fig 1.3). The amino acid sequence further dictates the final 3-D structure of the protein [9].

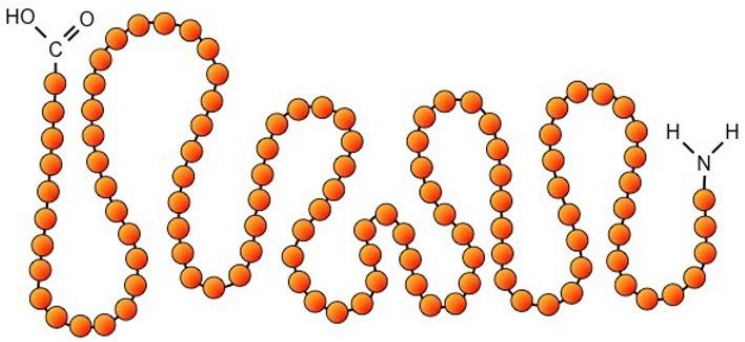

Figure 1.3. Diagram of the primary structure of the protein. Polypeptide chains of more than 50 amino acids are known as proteins. The beginning of the protein has the amine group intact (it is only bound to an amino acid on the carboxylic side) and is called the N-terminus and the end of the protein is called the C-terminus and it has the carboxylic acid group intact [11]. Figure adapted from Cornell B, 2016, BioNinja.

The protein's secondary structure consists of hydrogen bond interactions between the amine and carboxyl groups of the protein and causes folding. These structures are defined by the main chain dihedral angles (φ and ψ) or the torsion angles between backbone atoms [9]. This results in four main secondary structures: a) alpha helix, b) beta sheet, c) beta turn and d) random coil [12], a schematic of the secondary structures is shown in figure 1.4. These structures can range from three to five residues to over fifty residues in some coiled helices [9]. Alpha helices are formed when the backbone forms are right-handed helical conformation with 3.6 residues per turn [9]. Beta sheets consist of at least two beta strands resulting in an extended backbone conformation with dihedral angles confined to torsion angle φ between -60° and -180° and ψ torsion angle between 30° and 180°. Turns and loops are irregular secondary structures [9].

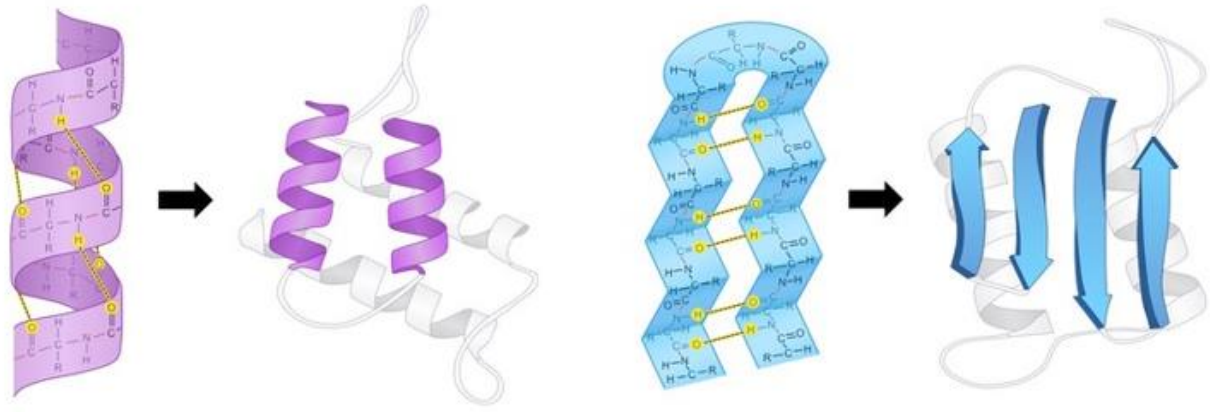

Figure 1.4. Diagram of the secondary structures of proteins. The purple diagram represents the alpha helical structure of the protein connected by random coils. In blue, the beta sheet and beta turns are represented [11]. Figure adapted from Cornell B, 2016, BioNinja.

The tertiary structure refers to the three-dimensional arrangement that results from hydrogen bonding, ionic bonding, dipole-dipole interactions, London dispersion forces, disulfide

bonds, and other non-covalent bonds [13]. These are a result of the R-group interactions and is the final structure for a single polypeptide chain as shown in figure 1.5.

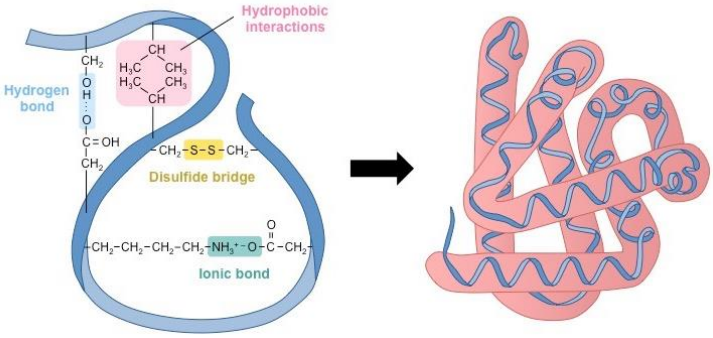

Figure 1.5. Diagram of the tertiary structure of a protein. The tertiary structure of the protein is determined by the interactions of the R-group of the amino acids with each other [11]. Figure adapted from Cornell B, 2016, BioNinja.

Proteins can also interact with each other. When multiple polypeptide chains interact, they experience interactions similar to the tertiary structure interactions. The bonding interactions are similar to the tertiary structure. A single protein chain is called a monomer. Proteins that have quaternary structures (made up of monomers) are called multimers as shown in figure 1.6.

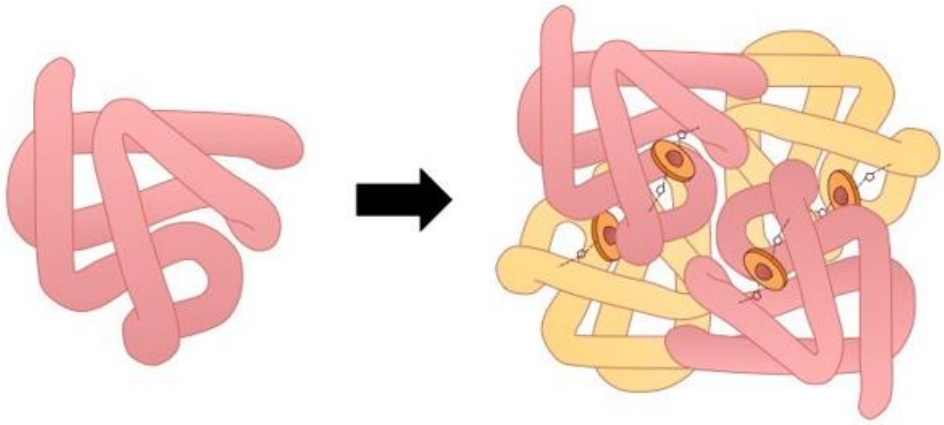

Figure 1.6. Diagram of the quaternary structure of a protein. The unbound R groups of individual polypeptide chains interact with other unbound R groups on other polypeptide chains to form a quaternary structure [11]. Figure adapted from Cornell B, 2016, BioNinja.

1.2 Membrane and Membrane Proteins

1.2.1 Cell Membrane

The cell membrane, also known as the plasma membrane, is a protective structure for the organelles of cells that allows it to maintain a fixed environment. It separates the interior of the cells from the outside environment. The semi-permeable membrane allows small molecules such as gases, lipids and other polar molecules to diffuse through the membrane, thereby regulating the transportation of materials into and out of the cell [14].

Plasma membranes are made up of a phospholipid bilayer. These phospholipids are made up of a hydrophilic head and one to two hydrophobic tails oriented so the tails experience hydrophobic interactions causing the heads to face the cytoplasm and the exteriors of the cells with the tails facing each other (see figure 1.7). The hydrophilic head consists of a negatively charged phosphate group and glycerol. The tails comprise of two fatty acid chains that are uncharged and

non-polar making them hydrophobic [15]. Throughout the membrane there are various lipids, proteins, glycolipids, and glycoproteins that all have various functions [14].

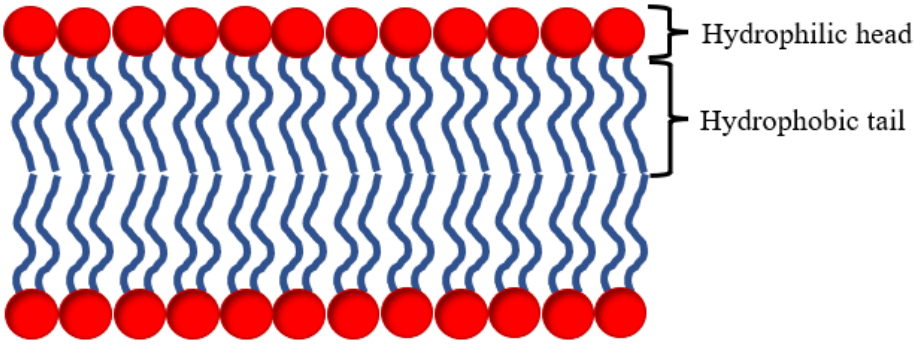

Figure 1.7. Diagram of the cell membrane. The hydrophilic head of the phospholipid (red) is oriented outwards to face the aqueous environments inside or outside of the cell, it consists of negatively charged phosphate and glycerol. The two hydrophobic tails (blue) are fatty acids that are non-polar and uncharged, oriented inwards to interact with each other and away from the aqueous environments [15]. This structure is known as the plasma membrane.

1.2.2 Membrane Proteins

Molecules that are too large to diffuse through the membrane must be transported through the membrane via channels. These channels are called membrane proteins which fall into two categories: peripheral membrane proteins, which are loosely attached to the lipid heads of the membrane or other proteins via electrostatic, covalent, or Van der Waals interactions and are therefore transient [16], and integral membrane proteins, which span the entire membrane and are permanently attached to the membrane [16]. Both integral and membrane proteins are shown in figure 1.8.

The two types of integral membrane proteins identified are α-helical and β-barrels. α-helical are the most abundant and most membrane proteins contain one or more helices that are typically 20 residues long and hydrophobic, thus allowing them to embed in the hydrophobic

portion of the membrane. β-barrels are β-sheets that form a barrel like structure [16]. The integral proteins, similar to phospholipids, have a polar (hydrophilic) portion that faces the cytoplasm and aqueous external environment of the cell and a non-polar portion (hydrophobic) that interacts directly with the hydrophobic tails of the bilayer and helps anchor the protein to the membrane [17].

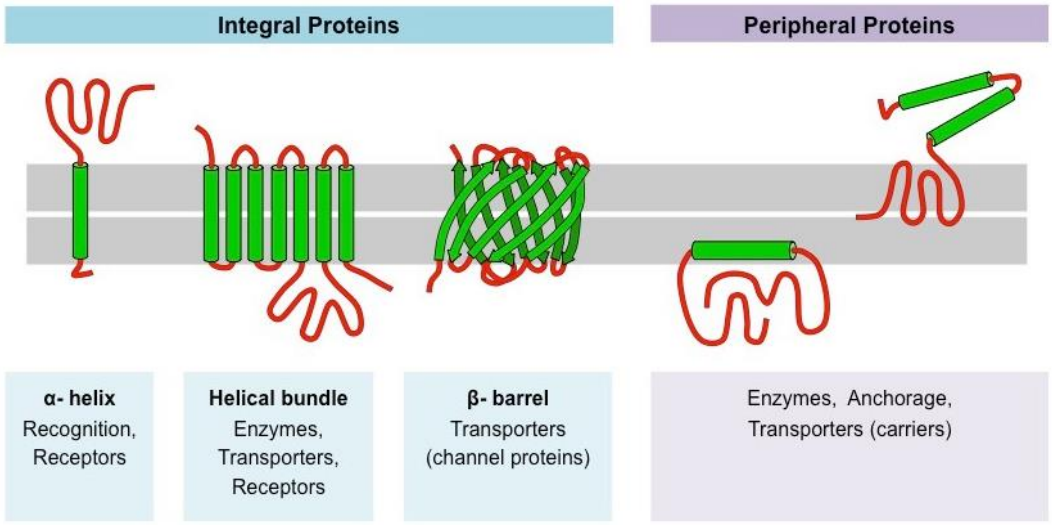

Figure 1.8. Diagram showing the different types of membrane proteins. The green cylinders represent α-helices, the green arrows represent β-sheets, and the red loops represent random coils. Integral proteins are fully embedded in the membrane (grey) and act as more permanent structures in the membrane. Peripheral proteins are generally more transient and can often move throughout the membrane [17]. Figure adapted from Cornell B, 2016, BioNinja.

Generally, membrane proteins execute a variety of functions. The proteins can act as junctions to connect two cells together, they can fix enzymes to membranes to constrain metabolic pathways, act as markers for cellular identification, and to connect proteins to the cytoskeleton and extracellular matrix. Membrane proteins also facilitate diffusion and active transport as well as function as receptors for peptide hormones and other types of ligands [17].

1.3 G Protein-Coupled Receptors (GPCRs)

G protein-coupled receptors (GPCR) are one type of integral membrane protein, used by cells to convert extracellular stimuli to intercellular reactions. There are three main regions of GPCRs: the extracellular region, the seven transmembrane portions, and the intracellular regions [18]. The extracellular region modulates the entry of ligands that range from small molecules to large proteins. The transmembrane domains provide the stability of the protein and binds to ligand. The intercellular regions of the GPCRs bind to a trimer known as a G protein which activates various signals in the cells [18].

These receptors belong to one of the largest families of membrane proteins. This family of membrane proteins are characterized by their seven helical transmembrane (spans the membrane) regions connected by inter- and extra- cellular loops [19] as shown in figure 1.9. They are further categorized into six families due to similarities in sequence and structure: family A- rhodopsin, family B- secretin receptor, family C- metabotropic glutamate, family D- fungal pheromone P and α-factor receptors, family E- fungal pheromone A and M factor receptors, and family F- cyclic AMP receptors from Dictyostelium (eukaryotic bacterivores). Families A-C contain other receptors that are not rhodopsin, secretin- receptor and metabotropic glutamate receptors but share similarities in structure [20].

GPCRs are often the target for drugs due to the role in mediating the bodies physiological responses to hormones, neurotransmitters, and external stimuli. GPCRs have been identified in the pathogenesis of diseases such as Alzheimer's disease [18] and cancer cell proliferation [21].

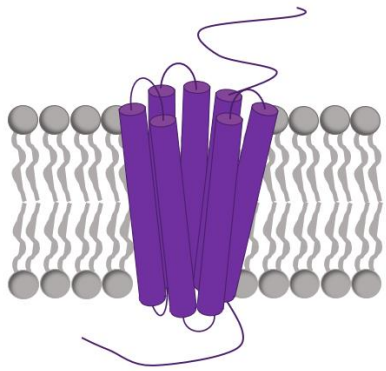

Figure 1.9. Diagram of a G protein-couple receptor. All GPCRs have the same basic structure regardless of the family it belongs to. The seven α-helical transmembrane domains (purple cylinders) interact hydrophobically with the fatty acid tails of the plasma membrane (grey). They are joined together with inter and extra cellular loops which reside on either side of the plasma membrane, in either the cytoplasm or the outside of the cell.

GPCRS are the largest family of membrane proteins and are responsible for most cellular responses to chemical stimuli like hormones and neurotransmitters, as well as physical stimuli such as vision, olfactory modality, and taste [19].

Class A GPCRs, also known as rhodopsin-like family consist of more than 700 members. They are further divided into 10 subgroups: aminergic, peptide, protein, lipid, melatonin, nucleotide, steroid, alicarboxylic acid, sensory, and orphan, depending on various similar structural characteristics between subgroups. Due to their wide range of physiological functions, class A GPCRs are therapeutically, the most targeted family of GPCRs. Structurally, they are similar to other classes of GPCRs with 7 helical transmembrane domains. Additionally, one of the domains forms a pocket for ligand binding and the GPCR family contains an extra eighth helix with a palmitoylated cysteine at the C terminal. One such group of receptors belonging to the class A GPCRs are the human muscarinic acetylcholine receptors [22, 23].

1.3.1 Ligands and Ligand Binding

For these cellular responses to occur, the GPCR must be activated usually by some ligand. A ligand is a biological molecule that binds to a receptor and causes a change in cellular signaling [24]. When the ligand binds to the receptor, the receptor undergoes a conformational change to prevent dissociation (see figure 1.10). Ligand binding can be orthosteric, where the ligand binds at the active site, or it can be allosteric, where the ligand binds elsewhere on the protein surface and changes the conformation of the protein binding site [25]. Once this conformational change occurs, the heterotrimeric G protein (Gα, Gβ/Gγ) is activated. The exchange of GDP/GTP (guanosine diphosphate/triphosphate) associated with the Gα unit, causes Gβ/Gγ to dissociate from the Gα. These subunits are then free to initiate intracellular signaling responses by interacting with other downstream effectors. The signals tend to be perceived at the membrane level and are therefore, the transmembrane events likely routes for signal generation and transduction [26].

Figure 1.10. Diagram of a GPCR bound to a ligand orthosterically. Ligands (cyan) can bind to the active site of the GPCR, sometimes by embedding itself into the transmembrane domains, and cause conformational changes in the structure of the GPCRs. These conformational changes activate the GPCR and cause a number of reactions depending on the type of ligand, the family of GPCR, and the location of the GPCR.

During drug development, the effects of ligands are studied to either mimic or prevent the cellular functions activated by the ligands. These effects can be broken down into three groups: agonist, antagonist and inverse agonist. Agonist effects replicate the activation of the receptor, similar to a natural ligand. These resulting action of receptor due to the presence of the ligand can be full, which produces the maximum effect, or it can be partial, which produces a detectable but not maximal effect. Inverse agonists produce the opposite effect of the agonist and can either be

full or partial inactivation. Antagonists on their own do not cause a reaction but will negate the effects that the agonist and inverse agonist have [27].

GPCR ligands are typically agonists and are physically and chemically diverse. Ligands can be both natural and synthetic and produce a range of effects on the body. Ligands include: ions (K^+, Na^+), vitamins, tastants, odorants, peptidic and other types of hormones (estrogen), proteins (chemokines), natural products (morphine), neurotransmitters (acetylcholine), etc. This diversity in family of ligands makes GPCRs are therapeutic target for many drug companies [28].

1.3.2 The Human Muscarinic Acetylcholine Receptors

The human muscarinic acetylcholine receptors regulate the response of the central and peripheral nervous systems to the neurotransmitter, acetylcholine. The muscarinic receptors are a class A rhodopsin-like GPCR, due to its structural similarities to rhodopsin, and has five subtypes, M1R-M5R. The muscarinic receptors are further subdivided into two functional groups depending on the receptor's selectivity for particular G proteins. M_1, M_3, and M_5 selectively couple to G_q class G proteins and M_2 and M_4 selectively couple to G_i class of G proteins [29]. This family of GPCRs are present in almost all organs, tissues and cell types. Muscarinic receptors present in the central nervous system regulate many cognitive, behavioral, sensory, motor and autonomic functions [29]. Malfunctions in these receptors have been linked to major diseases such as Alzheimer's disease, Parkinson's disease, depression, schizophrenia and epilepsy [4, 29].

The M_2 muscarinic acetylcholine receptor is necessary for the physiological control of the cardiovascular function [30]. The M_2 receptor is the main muscarinic receptor found in the heart and activates the parasympathetic nervous system to decrease heart rate and reduce atrial contraction [30].

As with all GPCRs, the M_2 receptor comprises of seven α-helical transmembrane domains (TM) interconnected with intra-cellular and extra-cellular loops. The M_2 receptor is also characterized by its large third intracellular loop (ICL) connecting TMs 5 and 6 (see fig 1.11). This loop has a flexible structure and plays a key role in the sensitivity of coupling G-proteins to the M_2 receptor [31]. The ILC3 also functions as a site for agonist and other second messenger systems, as well as tending to be involved in protein-protein interactions [31].

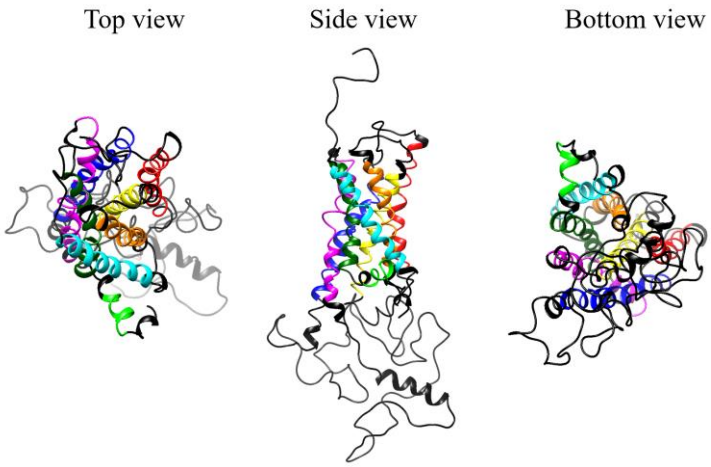

Figure 1.11. Diagram of the human muscarinic receptor M_2. Each transmembrane domain (TM) is represented by a color. TM1: cyan, TM2: orange, TM3: yellow, TM4: red, TM5: blue, TM6: magenta, TM7: dark green, and helix 8: green. Each TM domain is connected by a black intra or extracellular loop. The top view is from the extracellular domain, side view is within the plasma membrane and bottom view is from the cytoplasmic domain. The large third intracellular loop is a long flexible random coil structure consisting of approximately 180 amino acids. Structure of M_2R generated using UCSF Chimera, developed by the Resource for Biocomputing, Visualization, and Informatics at the University of California, San Francisco, with support from NIH P41-GM103311

1.4 Oligomerization

Self-association is a biological event that affects the structural and functional properties of proteins. While some proteins form more permanent quaternary structures like hemoglobin, other proteins may associate and dissociate forming a more transient structure called an oligomer such

as dimers (pairs of proteins) and higher orders [32]. Oligomerization often results in new functions or improves existing functions and is generally controlled and influenced by external factors such as macromolecular crowding, variations in ionic strength, and changes in pH and temperature [33]. Proteins can interact with identical proteins to form homo-oligomers such as collagen (as seen in figure 1.12) or it can interact with different types of proteins to form hetero-oligomers.

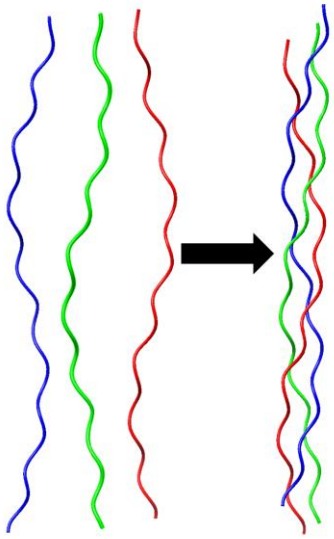

Figure 1.12. Diagram of Collagen as a homo-oligomer. The polypeptides of collagen have a glycine as every third residue. Three individual but identical strands of these polypeptide chains bind together to form the protein collagen. Structure of collagen generated using UCSF Chimera, developed by the Resource for Biocomputing, Visualization, and Informatics at the University of California, San Francisco, with support from NIH P41-GM103311

Some functions of homo-oligomers include cell-cell adhesion, regulations of gene expression, activity of enzymes, ion channels, and receptors [34]. Homo-oligomers sometimes undergo reversible transitions between conformations to preserve symmetry of the complex and account for allosteric mechanisms in signal transduction and cooperative binding [35]. Additionally, proteins can form large stable structures without increasing genome size [34].

1.4.1 Oligomerization of G Protein-Coupled Receptors

Recent developments in GPCR research presents both that most, if not all, GPCRs can homo-oligomerize or hetero-oligomerize. Oligomerization of GPCRs can affect receptor binding and other activities depending on what type of receptors are interacting [36]. Initially, non-radiative techniques were used to study homo- and hetero- oligomerization of GPCRs. In 1975, a studyby Limbird and Lefkowitz demonstrated oligomerization as site-site interactions among the β_2-adregenegic receptors [37]. Other studies conducted using the same receptor used radiation inactivation, cross-linking, photoaffinity label, and co-immunoprecipitation to provide biochemical evidence for oligomerization [7]. In the 1990s, trans-complementation, and dominant-negative and – positive effect studies were conducted on chimeric and mutant receptor constructs to reveal GPCR oligomerization. Studies showed that the chimeras had no binding activity individually but ligand binding activity comparable to wild type when co-expressed [7]. Other studies reported different functional effects of molecular interactions among GPCRs [7]. Western blot experiments paired with immunoprecipitation using antibodies provided the first direct evidence of homodimerization of β_2-adregenegic receptor and hetero-oligomerization of serotonin receptors with lysophosphatidic acid receptors 1 and 3 and γ-aminobutyric acid B_2, dopamine D_1 and D_2 receptors and α_{1b} and β_2 adrenergic receptors [7].

Resonance energy transfer (RET) techniques have gained popularity in recent decades and provide the best resolution for direct oligomerization studies [7]. Techniques such as bioluminescence RET (BRET) and fluorescence RET (FRET) are widely used and are advantageous due to their high signal to noise ratios, precise targeting of receptors, uses of intact and often live cells, and quantification of proportions of oligomers formed. Some drawbacks include potential bleed through of artifacts and signals being non-discriminate between non-mature

and mature proteins [7]. These approaches have led to the discovery of a variety of GPCRs as oligomers including but not limited to dopamine D_2, thyrotropic, opioid, and yeast α-factor receptors.

Chapter 2

FLUORESCENCE BASED DETECTION TECHNIQUES

In this chapter, the structure, photophysical properties, and use of some fluorescent proteins in fluorescence microscopy and FRET are reviewed.

2.1 Fluorescent Proteins

Fluorescent proteins were discovered in the early 1960s by researcher, Osamu Shimomura, studying bioluminescent Aequorea Victoria jellyfish [38]. They isolated the blue-light-emitting bioluminescent protein called aequorin as well as another protein that was eventually called the green fluorescent protein. In 1992, Douglas Prasher, cloned and sequenced the cDNA and genomic clones of GFP from the Aequorea Victoria jellyfish [39]. It was then used for monitoring gene expression and protein localization in prokaryotic and eukaryotic cells [40]. Roger Tsien, a chemist at the University of California, San Diego, then probed the proteins primary, secondary, tertiary and quaternary structure and created a full palette of fluorescent proteins[41, 42].

From this original protein, many variations have been engineered including blue, cyan, and yellow variants, which was further expanded to include red, orange, and far-red variants [43]. It is useful due to its stability and because the chromophore does not need a cofactor due to the process of its formation [44].

Fluorescent proteins are approximately 25kDa (1 Dalton = 1.66e-27kg) in mass. The entire protein is essential for the maintenance of fluorescence. It consists of a rigid β barrel fold made up of 11 β sheets surrounding a central α helix as shown in figure 2.1. The fluorophore is made up of three amino acids: serine, tyrosine and glycine located at locations: 65, 66, 67, and located at the

center of the sheets. The fluorophore can be mutated to respond to and emit at a variety of excitation wavelengths across the visible spectrum [45].

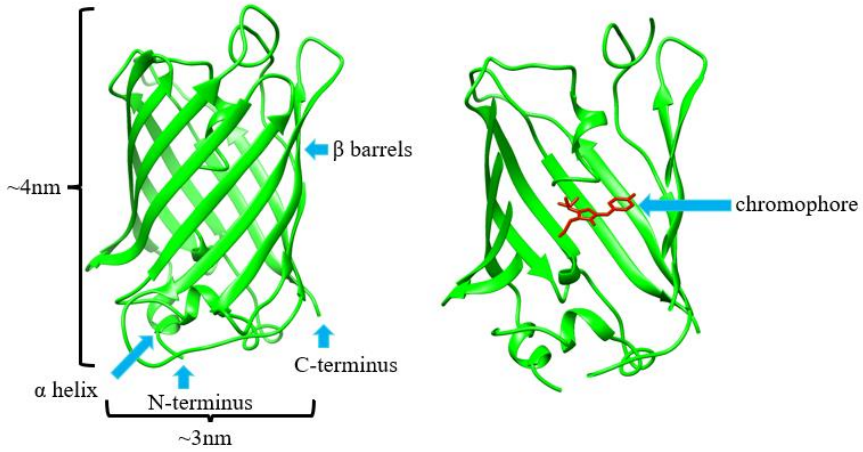

Figure 2.1. Diagram of the green fluorescent protein. The structure of the green fluorescent protein derived from the Aequorea Victoria jellyfish consists of 11 β sheets surrounding an α helix. The protein is approximately 4nm in height and approximately 3nm in diameter. The chromophore (red) is located in the α helix at residues 65, 66, and 67. For the green fluorescent protein, the residues are serine, tyrosine and glycine. These amino acids can be genetically modified to change the fluorophore to react to various wavelengths of light. Structure of GFP_2 generated using UCSF Chimera, developed by the Resource for Biocomputing, Visualization, and Informatics at the University of California, San Francisco, with support from NIH P41-GM103311.

2.2 Fluorescence-Based Detection of Proteins

Fluorescence microscopy is a unique method to study both live and fixed cells with a high level of sensitivity and specificity using a variety of fluorescent indicators [46]. This approach is based on the phenomena that fluorescent molecules emit fluorescent light after being excited. Images of biological molecules can be obtained from the fluorescence detected by fluorescence microscopes [47]. A variety of experimental techniques are based on fluorescence microscopy, such as protein motion tracking [48], protein colocalization [49], photobleaching step counting (PSC) [50],

fluorescence recovery after photobleaching (FRAP) [51], fluorescence resonance energy transfer (FRET) [52], and fluorescence lifetime imaging microscopy (FLIM) [47, 53].

Repetitive excitation can damage fluorescent molecules or they undergo non-radiative decay prior to the light emission [47].The fluorescent proteins absorb the light and enter an excited state. After vibrational relaxation, the fluorescent protein can either release a photon, as shown in figure 2.2, and return to the ground state or transfer its energy, non-radiatively, to the environment or another fluorescent protein.

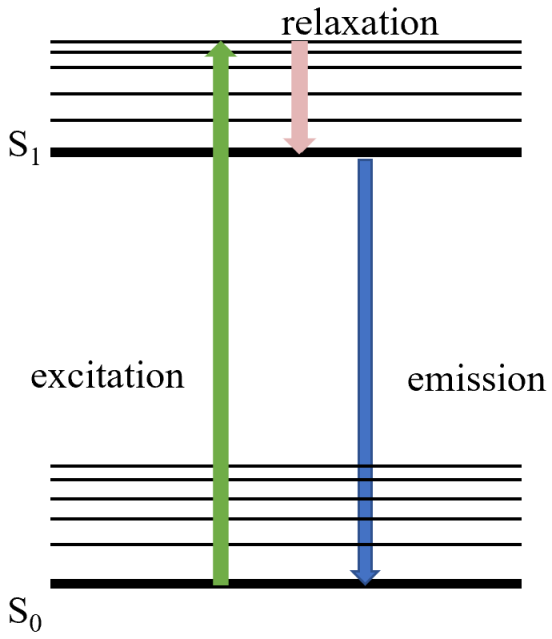

Figure 2.2. Schematic representation of fluorescence. A molecule in the ground state (S_0) can be directly excited to the first excited state (S_1). After vibrational relaxation, it can return to the ground state by releasing a photon. The time for this process is known as the fluorescence lifetime.

Fluorescence-based detection techniques can be broken down into single molecule type and ensemble-based approaches. Single molecule approaches are protein motion tracking, protein colocalization, and photobleaching step counting. Other fluorescence-based approaches, include

fluorescence recovery after photobleaching (FRAP), the related fluorescence loss in photobleaching (FLIP), fluorescence localization after photobleaching (FLAP), fluorescence resonance energy transfer (FRET), and fluorescence lifetime imaging microscopy (FLIM) [47, 53].

For single molecule studies, a common and powerful method for tracking protein motion in live or fixed cells uses the center of the point spread function of the microscope from fluorescence micrographs tagged with fluorophores [47]. One of these methods is fluorescence imaging with one-nanometer accuracy (FIONA). In a study conducted by Kural et al, fluorescence based real time localization techniques with 1nm spatial resolution and 1ms temporal resolution was used to study the molecular motors myosin V, myosin VI, kinesin and dynein [54]. The center point of an object can be confined if the center point of the emission pattern is determined. The diffraction pattern of light from objects like membrane organelles and fluorescent beads, can be fit with a two dimensional Gaussian fit to resolve the PSF with 1nm accuracy and localize different sub-wavelengths [54].

Another fluorescence microscopy tool that is used to study cellular functions of proteins and other molecules is protein colocalization [49]. Despite not being an extremely high-resolution technique, it can be used to determine whether two molecules associate with the same structures, an example being if a particular protein associates with mitochondria [40]. Colocalization consists of two components: co-occurrence and correlation, co-occurrence is the spatial intersection between two probes and correlation uses the spatial overlap and codistribution between structures [49]. For analysis, there are a variety of metrics such as Pearson's Correlation Coefficient, Manders Overlap Coefficient, and Manders Colocalization Coefficient as outlined in a reviewby Dunn et al [49].

When studying proteins, counting discrete photobleaching steps in fluorescence microscopy is ideal. Photobleaching occurs when fluorophores are exposed to light over time and are irreversibly photochemically transitioned to a non-fluorescent state [50]. The stoichiometry of proteins in a molecular assembly can be assessed by counting photobleaching steps. This analytical approach uses proteins tagged with fluorophores, activating them and observing the fluorophores bleach therefore determining the number of subunits in a complex [50].

Fluorescence recovery after photobleaching is a technique developed by Axelrod et al [55] that measures the rate of fluorescence recovery at a previously bleached site to study protein mobility [47]. Fluorescent molecules are photobleached in a small area using high intensity light from a focused laser beam. The diffusion of the non-bleached fluorophores from the surrounding area at specific velocity leads to recovery of fluorescence. Originally, it was used to measure diffusion in cell membranes using organic dyes. However, with the advent of confocal microscopy, it became more popular to study protein mobility in the interior of cells [47]. FRAP can generally be used to study protein movement and diffusion speed, compartmentalization and connections between intracellular compartments, protein exchange speed and binding characteristics between proteins [47].

Another fluorescence-based detection technique is fluorescence loss in photobleaching (FLIP) [56], a method that is complementary to FRAP. FLIP uses repetitive bleaching of an area adjacent to an unbleached area. The diffusion of the bleached molecules into the unbleached area is measured and determines the mobile fraction of fluorescent molecules [47]. The incomplete loss of fluorescence defines the immobile fraction of proteins that do not move to the non-bleached area. If molecules do not become bleached, it suggests that they are confined to a cellular compartment making FLIP useful for determining connectivity between different regions of the

cell and for studying the exchange of molecules between two compartments [47]. FLIP and FRAP can further be combined to study different dynamic properties of proteins and determine mobility of different proteins.

Since bleached molecules cannot be visualized, FLIP and FRAP are not always the most efficient tool to study the dynamics of unbleached molecules. Fluorescence localization after photobleaching is a technique developed by Graham Dunn, where the molecule carries two fluorescent labels. One is locally bleached, and the other is used as a reference label and can be imaged independently or simultaneously using fluorescence microscopy [47]. The absolute FLAP signal is obtained by subtracting the bleached signal from the unbleached signal and allows the labelled molecule to be tracked as well as be used to calculate the photobleached fraction of molecules within each pixel [47]. Förster resonance energy transfer (FRET) is explored more in depth in the following section.

2.3 Förster (or Fluorescence) Resonance Energy Transfer (FRET)

Förster resonance energy transfer, also known as fluorescence resonance energy transfer (FRET) is the non-radiative energy transfer from an excited fluorescent donor molecule to a nearby unexcited acceptor molecule via dipole-dipole interaction [52] This phenomenon provides spatial information of molecules in relation to each other. The FRET efficiency is given by [57]

$$E = \frac{R_0^6}{R_0^6 + r^6}, \tag{2.1}$$

where r is the distance between donor and acceptor and R0 is the Förster distance (or radius) [52]. According to Eqn. (1), the energy transfer is highly efficient when the intermolecular distance is comparable to the Förster distance, i.e., where the latter is given by the expression [47]

$$R_0 = [2.8 \times 10^{27} \kappa^2 Q_D \varepsilon_A J(\lambda)]^{\frac{1}{6}} \tag{2.2}$$

where Q_D is the fluorescence quantum yield of the donor in the absence of the acceptor, ε_A is the maximal acceptor coefficient ($mol^{-1}cm^{-1}$), J(λ) is the spectral overlap integral between the normalized donor fluorescence ($f_D(\lambda)$) and the acceptor excitation spectra ($\varepsilon_A(\lambda)$), and κ^2 is the dipole orientation factor. The spectral overlap integral and the dipole orientation factor are given by the equations [47]

$$J(\lambda) = \int_0^\infty f_D(\lambda)\varepsilon_A(\lambda)\lambda^4 d\lambda \quad (2.3)$$

$$\kappa^2 = [sin\theta_D sin\theta_A cos\varphi - 2cos\theta_D cos\theta_A]^2 \quad (2.4)$$

FRET depends on the angle between both chromophores and varies between 0 and 4. When the transition dipoles of both chromophores are parallel to each other, there is maximum FRET whereas when the chromophores are perpendicular the is negligible FRET. Assuming that both chromophores have the maximum degree of freedom, therefore a free to rotate and are isotropically oriented during excitation, average value overall values is defined as 2/3 [47].

Fluorescent molecules that have been excited from the ground state can lose their energy radiatively or non-radiatively and can be represented using the rates of excitation and de-excitation ($\gamma^{ex,\ r,\ or\ nr}$) of the donors and acceptors as shown in figure 2.3.

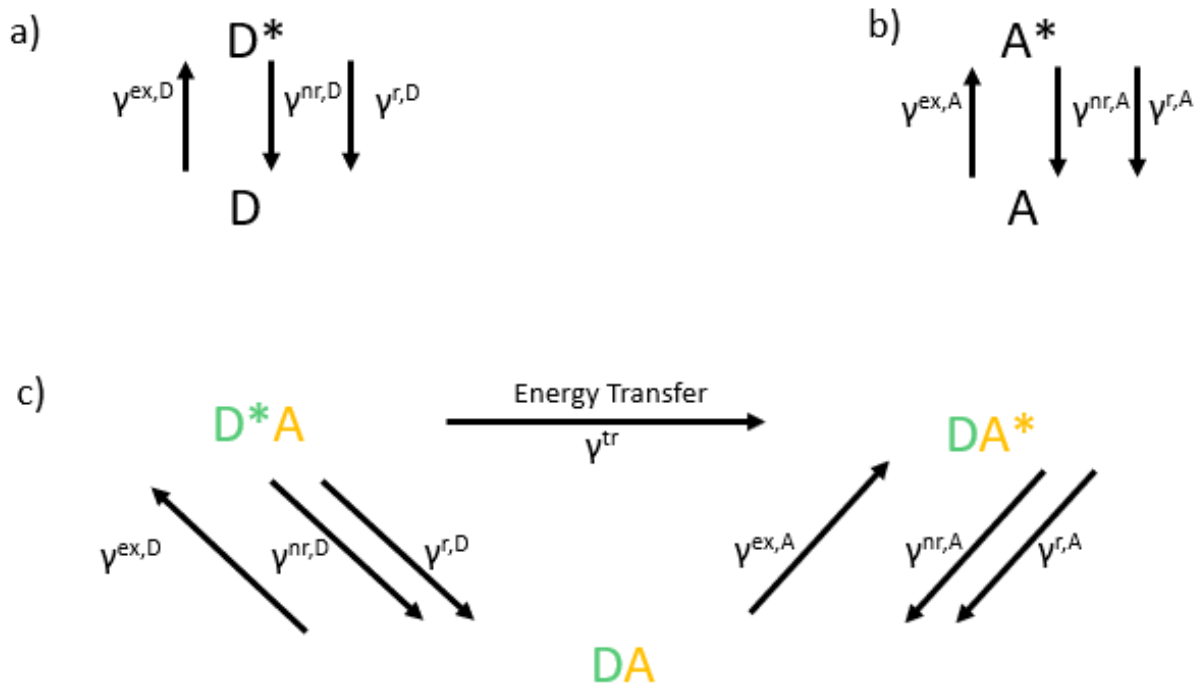

Figure 2.3. Schematic of the energy transfer process between a donor and acceptor. γ^{X} is the rate of excitation (ex) or de-excitation either radiatively (r) or non-radiatively (nr) of the donor (D, green) and acceptor (A, yellow) molecules. The asterisk denotes the species that are in the excited state. a) Donors that are directly excited from the ground state to the first excited state can lose their energy either radiatively, via a releasing a photon, or non-radiatively via heat or vibrational losses. b) Acceptors can also be directly excited from the ground state and lose their energy in a similar fashion. c) Excited donors in the presence of acceptors, now have an alternative non-radiatively path for losing energy in the form of FRET. Acceptors can now enter the first excited state via FRET as well as through direct excitation of the acceptor. Figure adapted from Raicu, 2019 [58]

FRET has been adopted as a spectroscopic ruler [59] to monitor various molecular activities that produce changes in distances such as protein-protein interactions and conformational changes. One advantage of the technique is that it is minimally invasive and non-destructive to live cells. There are two types of fluorescent molecules used in FRET: the intramolecular type where the donor and acceptor molecules are conjoined to the same molecule so that conformational

changes in the molecule induce changes in FRET and the intermolecular type where two or more independent molecules are tagged with FRET biosensors so intermolecular interactions cause changes in FRET [57].

Choosing the right FRET pair is critical in optimizing FRET biosensing. The first criterion to choosing a good FRET pair is significant overlap between both donor and acceptor emission spectrum [60]. Secondly, the Förster distance between pairs must be detectable by the experimental instruments [60]. Thirdly, the excitation wavelength of the donor should cause negligible direct excitation of the acceptor [60]. Other criteria such as labeling chemistry, charges, size of the donor and acceptor and more should be considered [60]. There are three main types of fluorophores that are used as FRET biosensors: fluorescent proteins (FP), organic dyes, and quantum dots [61]. There are many advantages to using fluorescent proteins over the other two. Since fluorescent proteins are genetically encoded, it is easy to build the biological system using genetic engineering by fusing the fluorescent protein to the sensing domains whereas organic dyes and quantum dots need antibodies to be present in order to label the sensing domain [62]. Additionally, producing stable cell lines expressing the biological systems using fluorescent proteins are easily achievable and FP based FRET pairs are generally stable in cells for a long time [61]. FP based FRET pairs can be introduced into cells in vivo and in vitro through transfect or virus infection, an easier process than introducing organic dyes and quantum dots [57].

There are a variety of FP based FRET pair types to choose from, including cyan-yellow FP (CFP-YFP) FRET pairs, green-red FP (GFP-RFP), far-red-infrared FP (FFP-IFP) and many others each with its own advantages and shortcomings [57, 63]. For this study, green fluorescent protein (GFP_2) and yellow fluorescent protein (YFP) were used as the FRET pair. YFP has a high absorption and quantum yield which makes it an attractive FRET acceptor. The FRET efficiency

can be determined using techniques such as spectral unmixing to separate the signal from the donor and acceptor. Spectral unmixing uses the emission signatures of the two spectra to determine their individual contributions to the signal and allows GFP_2 and YFP to be used despite their spectral overlap [58]. The integrals of the GFP_2 and YFP spectra, the quantum yields of the donor and acceptor and the signal of the donor and acceptor at each pixel was used to calculate the FRET efficiency at each pixel using the process described in Chapter 3, section 3.6 "Calculation of apparent FRET efficiency using spectral resolution" [64, 65].

2.4 Fluorescence Lifetime Imaging Microscopy (FLIM)

There are a variety of fluorescence techniques that have been applied to live biological systems due to their high sensitivity and non-invasiveness. Data from these techniques are generally obtained in the three spatial dimensions over various wavelengths [66]. However, the spatial distribution of the fluorescence intensity and fluorescence spectra are not the only characteristics of fluorescence, there is also the decay function. A molecule in the excited state can return to the ground function by releasing a photon, by converting the energy into heat, by giving the energy to the environment, or by crossing into a triplet state and returning to ground from there [66]. The resulting fluorescence decay is generally a single exponential function for a homogeneous population and the rate constant is the fluorescence lifetime of the molecule. This rate constant is dependent on the type of molecule, its environment and its conformation [66].

Fluorescence lifetime imaging microscopy (FLIM) is an imaging technique that extracts the fluorescence lifetime of a fluorescent molecule (i.e., the time that a fluorophore is in an excited states before radiatively releasing its energy) from the fluorescence decay following excitation with a pulsed laser and is used to non-invasively study the molecular environment [67]. FLIM

techniques can be used to perform FRET measurements. Since FRET provides an alternative de-excitation pathway, the presence of an acceptor molecule can affect the fluorescence lifetime of donor molecule. The donor molecule can non-radiatively transfer its energy to the acceptor molecule which can in turn fluoresce [68]. Theoretically, the longer the donor molecule spends in the excited state, the more likely it is to transfer its energy via FRET, so donor fluorescence and energy transfer are considered competing processes[68]. In the absence of FRET, the donor lifetime is unchanged because there is no alternative de-excitation pathway, however in the presence of an acceptor within Förster distance, the donor can lose its energy to the acceptor via FRET, thus shortening the fluorescence lifetime of the donor. The various pathways of de-excitation are illustrated in figure 2.4.

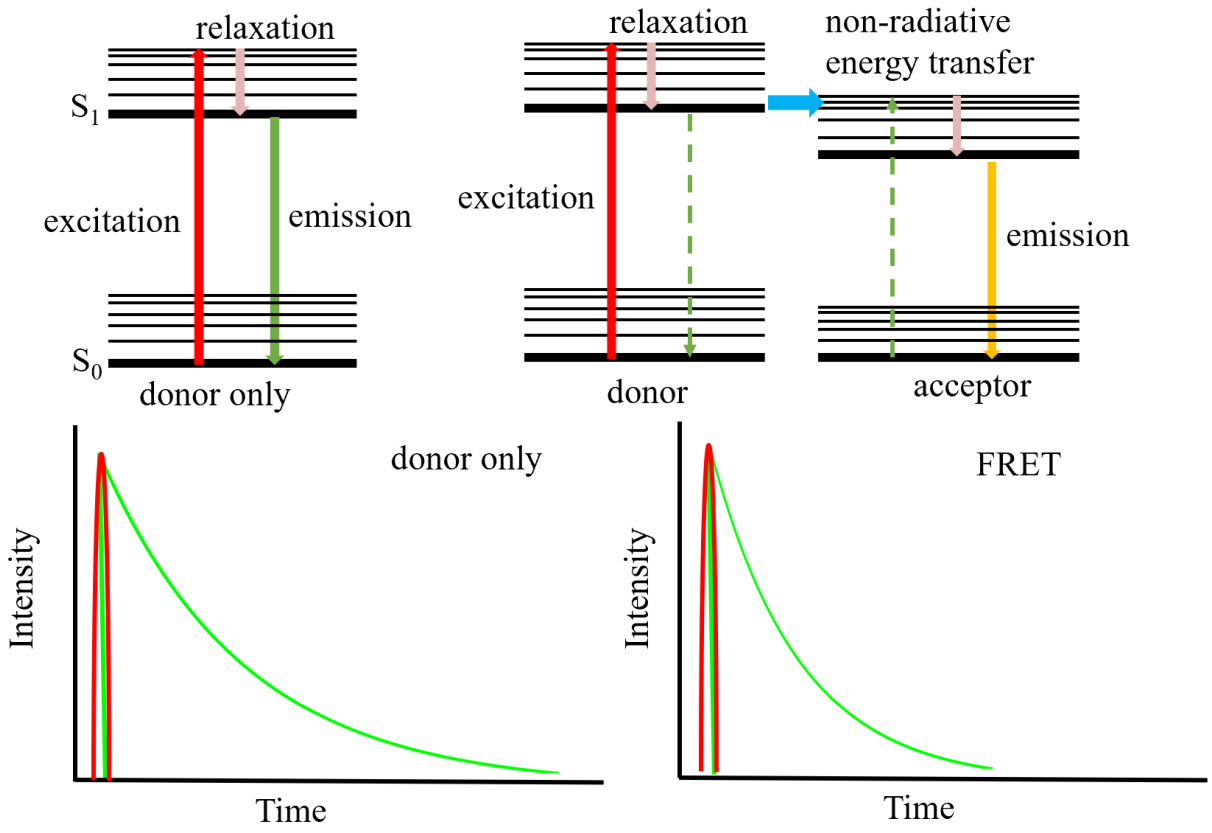

Figure 2.4 Schematic showing the shortening of the donor lifetime due to FRET. When the donor is excited to the first excited state, it returns to the ground state by emitting a photon. This process of fluorescence decay is a single exponential function for a homogeneous species. In the presence of an acceptor, the donor molecule can non-radiatively transfer its energy to the acceptor molecule. This results in a shortening of the donor's fluorescence lifetime in the presence of the acceptor.

2.5 Oligomerization and FRET

Oligomerization is a biological event that occurs when proteins interact and associate with similar and dissimilar proteins. Protein-protein interactions can be studied using fluorescence-based detection techniques, such as FRET, FLIP [56], FRAP [69], and FLAP [47]. In a study by

McKenzie et al, FRET was used to study the dimerization and possible higher order oligomerization of the membrane protein, EphA2, a receptor tyrosine kinase and its response to the ligand ephrinA1-Fc [70]. The dissociation constants of the dimers and higher order oligomers were determined in order to assess the stability of the oligomers formed by EphA2. Fully quantified spectral imaging FRET (FSI-FRET), a method that yields two-dimensional membrane concentrations and FRET efficiencies [71], was used to obtain spectral data of EphA2. It was determined that the FRET efficiency does not only depend on the abundance of oligomers but also the distance between the fluorescent proteins.

A more advanced version of this method, dubbed FRET spectrometry [72], was introduced to study protein-protein interactions in living cells. The concept was introduced by Raicu et al [73] as FRET based method for finding the fraction of oligomers in a protein population and the size of the protein oligomers in each complex. Instead of the typical average-based approaches, FRET spectrometry uses the analysis of distributions of apparent FRET efficiencies of cells expressing the target protein across the image pixels [72]. Using a parameter that connects all the different configurations of donors and acceptors, termed *pairwise FRET efficiency*, E_p, the most probable quaternary structure of the oligomer is determined from the number of peaks in apparent FRET distribution as shown in figure 2.5 using the following equation [74].

$$E_{app} = \frac{1}{k}\sum_{i=1}^{k} \frac{n_{A,i}E_p}{1+(n_{A,i}-1)E_p} \tag{2.5}$$

This can be used to obtain information about the quaternary structure and stoichiometry of the target proteins.

Where $n_{A,I}$ is the number of acceptors within the range of the ith donor, k is the number of donors in the configuration, and E_p is the pairwise FRET efficiency.

These peaks can be used to create a unique FRET spectrum that corresponds to each configuration of the oligomers of the proteins and determine the oligomeric configurations of the protein [72, 73].

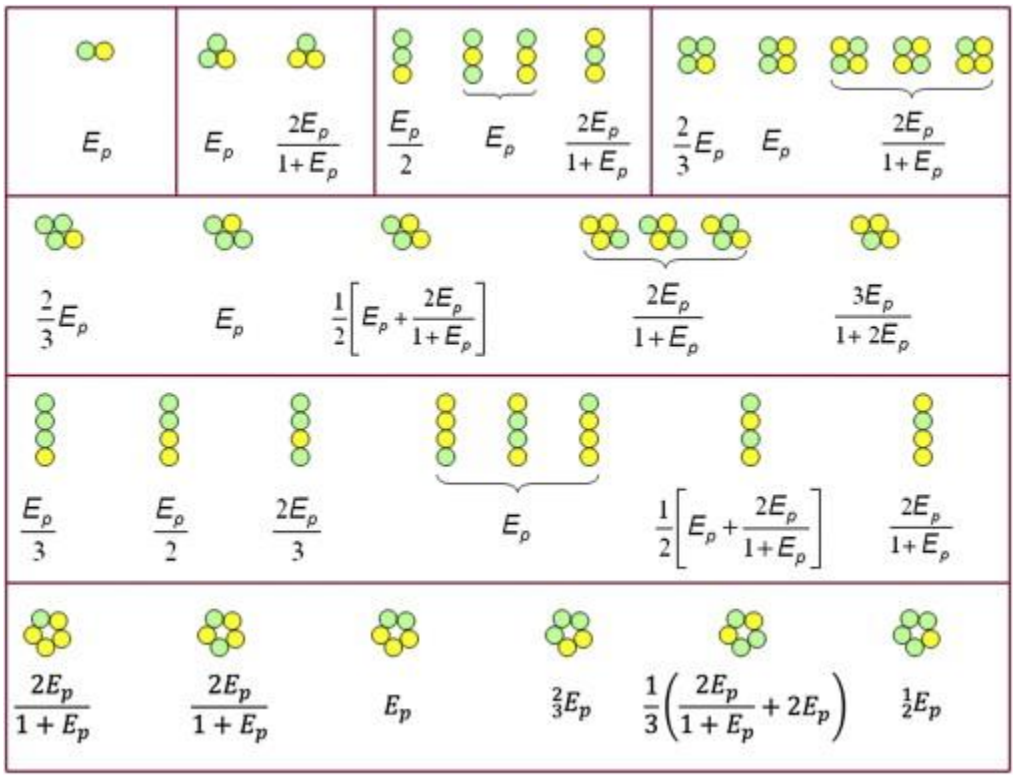

Figure 2.5. List of apparent FRET efficiencies for several differently sized and shaped constructs characterized by different configurations of donors and acceptors each. All FRET efficiencies depend on a single parameter, the pairwise FRET efficiency, E_p. Figure adapted from Raicu and Singh, 2013. [74]

Using spectrally resolved microscopes, emission spectra of the excited samples as well as images containing both donor and acceptor signal are collected. Pixel level FRET efficiencies are determined instead of the averages over multiple cells to account for heterogeneities of the distribution of the molecules of interest in the cell. There are various ways for donors and acceptors to be oriented within oligomeric complexes, and each configuration is characterized by an apparent

FRET efficiency. The aforementioned study used sterile 2 α factor receptor protein labelled with fluorescent proteins to present a theoretical model that relates FRET efficiency between a single donor and acceptor pair to the efficiency of energy transfer in protein populations [73]. Furthermore, using fluorescence imaging technology that has single molecule sensitivity, the stoichiometry and quaternary structures of membrane receptors and transporters in living cells can be determined with FRET spectrometry.

2.6 GPCR Oligomerization Studies

G protein-coupled receptors are a common target when investigating oligomerization. Both fluorescence-based detection techniques such as FRET, bioluminescence resonance energy transfer (BRET), and FRAP, as well as, biochemical experimental techniques such as co-immunoprecipitation, protein-fragment completion assays (PCAs), and blue-native PAGE (BN-PAGE) have been used to study homo- and hetero- oligomerization of GPCRs [69]. Oligomerization of GPCRs has also been involved in certain diseases. A study by Abdalla et al, identified altered heterodimerization of the angiotensin II receptor type 1 (AT_1) and bradykinin receptor B_2 associated with pre-eclampsia [75]. Mutations of the melanocortin-4 receptor (MC_4R) (D90N) gene has a negative effect on the WT-MC_4R/D90N heterodimer and is identified as one of the causes of early onset obesity [76].

Studies using FRET spectrometry to investigate oligomerization in GPCRs have also been conducted. In a study conducted by Paprocki et al, sterile 2 α-factor receptor (Ste2) were used to study oligomerization and conformational changes using FRET spectrometry **[64]**. The study found that Ste2 formed tetramers in the absence of the ligand α-factor pheromone and multiple distinct conformational substates in the presence of ligand. In a study conducted by Mishra et al, the types of oligomeric complexes formed by the rhodopsin receptors were investigated using FRET spectrometry**[77]**. This study aimed to determine whether mixtures of oligomeric complexes existed. Oligomerization of rhodopsin receptors was found to be concentration dependent with stable dimers and tetramers existing at low concentrations of receptors and higher order oligomers forming at higher concentrations **[77]**.

One of the earliest reported GPCR dimers was the heterodimer formed between the α2c-adrenergic receptor and the muscarinic acetylcholine M_3 receptor [78]. In the study conducted by Maggio, Vogel and Wess, chimeric receptors of the α_2/M_3 receptor determined that the receptors interact with each other at the molecular level [78].

There are other studies that have used fluorescence-based detection techniques to determine GPCR oligomerization. A study by Cottet et al, used BRET and time-resolved FRET to study GPCR oligomerization. Few techniques provide the spatial resolution required to determine molecular interaction with enough precision and the resonance energy transfer techniques are the most suitable [78]. Both BRET and time resolve FRET (TR-FRET) have a high signal to noise ratio and can perform multiplexing making them widely used techniques. This study found that GPCRs have a tendency to both homo- and hetero- oligomerize [79].

Class A, B, and C GCPRs were studied using single molecule FRET to determine oligomerization of these receptors in a study by Asher et al [80]. The μ-opioid receptor (MOR, class A), secretin receptor (SecR, class B) and the metabotropic glutamate receptor 2 (mGluR2, class C) were tagged with donor and acceptor fluorophores and imaged in real time using total internal reflection fluorescence microscopy [80]. The study concluded that mGluR2 formed stable dimers at all receptor densities while SecR required a high enough surface density in order to establish any long-lived interactions. MOR was found to exist only as a monomer regardless of the surface density [80].

Another type of receptor that has shown a tendency to oligomerize is the muscarinic family of receptors. The muscarinic receptors are class-A GPCRs which are responsible for a number of physiological roles associated with the central and peripheral nervous system. They have been established as a model for the study of GPCR structure and function. One study by McMillin et al, uses BRET to study the dimerization/ oligomerization of the M_3 receptor [81]. M_3 receptors were tagged with Renilla Luciferase 8 (RLuc8) or mVenus at the C terminus. Seven M_3-RLuc8 mutants were created and using BRET and other biochemical techniques, it was discovered that M_3-RLuc8 and M_3-Venus were found to dimerize, among other conclusions [81].

Another study by Goin and Nathanson, $M_{1\text{-}3}$ receptors were tagged with RLuc and YFP at the C terminal [82]. BRET and other biochemical techniques were applied to the constructs to study homo and hetero dimerization of the three muscarinic receptors. All three dimers were found to form homodimers with the M_1 homodimer being more stable than the M_2 and M_3 homodimers [82]. The study also found that coexpression of M_2 and M_3 receptors are susceptible to forming M_2/M_3 heterodimers that may facilitate M_3 receptor regulation [82]. In a study by Patowary et al, FRET spectrometry was used to study the homo-oligomerization of the muscarinic M_3 receptor

[83]. The complexes were found to form stable dimers and possibly interact to form tetramers and other higher order oligomers [83].

The focus of this study was the M_2 muscarinic receptor. Using fluorescence intensity-based microscopy, as well as fluorescence lifetime imaging, the size of an oligomer of M_2 receptors was determined. In the study conducted, by Pisterzi et al, M_2 receptors were tagged with eGFP, eYFP, or, eCFP, and using fluorescence microscopy techniques and FRET spectrometry analysis techniques, the M_2 receptors were found to form dimers and higher order oligomers [84]. Specifics regarding the configuration of the oligomers could not be determined using FLIM-FRET in this paper.

In this study, temporally resolved fluorescence-based techniques were used to conduct FRET spectrometry experiments on a biological system that was known to dimerize and form higher order oligomers, the M_2 receptor. One limitation of fluorescence lifetime-based FRET techniques is that there must be prior knowledge of the number of species present in the biological system. Typically, the pixel level data is fitted using one or two exponential curves to find the time constants. The number of exponential curves is directly related to the number of species in the pixel, for example, a homogenous biological system would be fit with a single exponential curve called a one-lifetime fit. This generally restricts FLIM-FRET techniques to biological systems with no more than two species. To overcome this limitation, the Raicu lab proposes a method that instead numerically integrates the signal from the time resolved data to calculate the FRET efficiency at the pixel level called tiFRET, outlined in chapters 3 and 4. Using FRET spectrometry analysis, metahistograms of the frequency vs. the apparent FRET efficiency of the M_2 receptor was determined and fit with a theoretical model in order to determine the size of the oligomer, and the overall geometry of the M_2 receptor oligomers.

Chapter 3

METHODS

In this section, the procedures performed for these experiments will be described, focusing on the technology and the analysis used for FRET imaging using temporal and spectral resolution as well as the analysis for both methods. Optical micro-spectroscopy (OptiMiS) is a unique technology developed by the Raicu Lab at the University of Wisconsin, Milwaukee and was used for the spectrally resolved experiments. A custom-built multiphoton workstation at the University of Wisconsin Laboratory for Optical and Computational Instrumentation (LOCI) was used for the temporally resolved experiments.

3.1 Cell Culture and Cell Sample Preparation

The materials needed for the cell culture and cell sample preparation are:

1) Dulbecco's modified eagle medium (DMEM) without sodium pyruvate supplemented with:
    a) 10% fetal bovine serum
    b) 2% L glutamine
    c) 1% penicillin streptomycin
2) Dulbecco's Phosphate-Buffered Saline (DPBS)
3) Trypsin
4) Trypan blue
5) Poly-D-Lysine
6) Distilled Water

48 hours (about 2 days) before imaging, approximately 150,000-200,000 cells were grown on plates coated with poly-D-lysine according to the procedure outlined below.

The wells of 2ml glass bottom imaging plates were coated with 330µl of poly-D-lysine and left for 1 hour. After 1 hour, the plates were rinsed thoroughly three times with distilled water and left uncovered to dry in the sanitized biosafety hood.

Incubated cells in a T25 flask were brought into the sanitized biosafety hood. The old cell media (DMEM) was removed by turning the flask upright and aspirating away from the cell growth. Cells were gently washed twice with 5ml of DPBS and the remaining DPBS was disposed. 0.5ml of Trypsin was added to the flask and the flask was incubated for 3 minutes. The bottom of the flask was gently tapped to remove cells from the surface. 5ml of DMEM was quickly added to the flask to prevent the cells from being poisoned by the Trypsin and gently shaken to suspend most of the cells. Cell media containing the unstuck cells were transferred to a 15ml Falcon tube for centrifugation for 5 minutes at 1400 rpm. Once centrifuged, the supernatant was removed leaving the cell pellet undisturbed. The pellet was then loosened and 1-2ml of DMEM was added. The hemacytometer was prepared by washing it with 70% ethanol and blotted dry. 90µl of Trypan blue solution was added to a 96 well plate and 10µl of suspended cells to the same well and 10µl of the diluted cell solution was pipetted onto the hemacytometer. Cells were counted and 150,000-200,000 cells were added to the dried treated glass bottom dishes with 2ml of DMEM and 800,000cells were added to a T25 flask with 5ml of DMEM. The dishes and the flask were returned to the incubator.

3.2 Transfection

For the time-resolved fluorescence imaging experiments, cells were transfected 24 hours before imaging, using a Lipofectamine 3000 Kit according to the manufacturer's protocol. Human muscarinic M2 receptor (M_2R) tagged with 2 ratios of green (GFP_2) and yellow (YFP) fluorescent proteins (1:1 and 1:3) and a plate with M_2R tagged with GFP_2 only were transfected into HEK293. For the spectrally resolved experiments, the same transfection ratios of a M_2R tagged with GFP_2 only, 1:1, and 1:3 were used as well as a plate of M_2R tagged with YFP only.

Transfection reagents that were used outlined below:

1) Plasmids expressing GFP2 and YFP attached to M_2R
2) Distilled water
3) Opti-MEM Media
4) Lipofectamine^{TM} 3000 Reagent
5) P3000 Reagent

Solutions of plasmids expressing fluorescent proteins GFP_2 and YFP attached to M_2R were diluted with distilled water so there would be a total of 2.5µg of DNA in each dish. The transfection procedure was initially split into two parts. 5-6 Eppendorf tubes were placed in the top and bottom rows of the Eppendorf tube holder as shown in fig. 3.1. In the top row, step a) 125µl of Opti-MEM Medium was added to each tube with 5µl of Lipofectamine 3000 Reagent and incubated at room temperature. In the bottom row, step b) 125µl of Opti-MEM Medium was added to each tube with 5µl of P3000 Reagent and 2.5µg of DNA and incubated at room temperature.

The solutions from part b) were added to the solution from part a) and incubated for 10-15 minutes at room temperature.

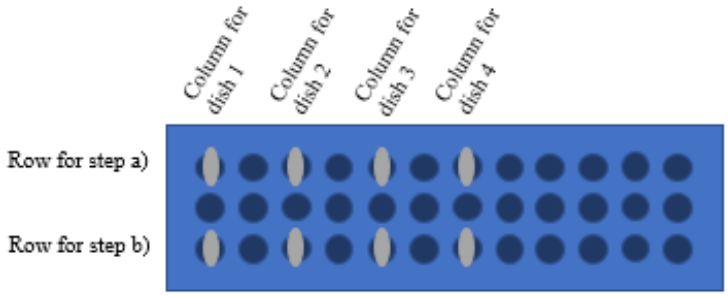

Figure 3.1. Schematic of the setup of equipment used during transfection. An Eppendorf tube rack was used to organize the transfection reagents and Eppendorf tubes for the two-step process. Row A is used for the first portion using Lipofectamine 3000 Reagent. Row B is for the second portion using P3000 Reagent.

After 15 minutes, the complexes were added to the plated HEK293 cells, and the dishes were incubated at 37°C with 5% CO_2. Transfected cells were imaged within 24-48 hours of transfection.

3.3 Time-resolved Fluorescence Imaging

Transfected cells were imaged in 2ml of DPBS using a multiphoton microscope with a Ti: Sapphire laser (Chameleon Ultrall, Coherent Inc., Santa Clara, CA) which was custom-built at the Laboratory for Optical and Computational Imaging (LOCI) in the Morgridge Institute for Research at the University of Wisconsin (Madison, WI) [85].

The multiphoton microscope from LOCI located at the University of Wisconsin, Madison consisted of:

1. Microscope: Nikon Eclipse TE2000U inverted microscope
2. SHG and MP Emission Detector: Hamamatsu H7422p-40 GaAsp photomultiplier (PMT)
3. Transmitted Light detector: An infrared-transmitting Si photodiode (Hamamatsu K34213) was used in a BioRad MRC-1042 Transmitted light detector box for detecting transmitted light.
4. Objectives: Nikon 60× Fluo Oil 1.4NA
5. Laser: Coherent Chameleon Ultra II Ti: Sapphire laser – tunable range 700-980nm
6. Scanning system: Cambridge Technologies 6210H galvanometer with Prairie Technologies (Bruker) galvanometer control box.
7. Laser power control via Pockel Cell: Conoptics Model 350-80LA KD*P Series Electro-Optic modulator with Model 302RM amplifier. Other power control schemes can be used as well.
8. Emission filters: Semrock 480/40 nm
9. Filter wheel: Sutter Instrument Lambda 10B Optical Filter Changer
10. Shutter: Uniblitz Model D122 shutter and driver system
11. Z and stage control: Applied Scientific Imaging MS-2000 xyz stage control
12. Vibrational table: TMC CleanTopII vibration isolation system

The multiphoton microscope setup, as shown in figure 3.2, located at LOCI lab at the University of Wisconsin, Madison, uses a femto-second laser that generates ultra-short pulses (100-fsec) at a repetition rate of 80MHz tuned to 800nm passed through an electro optic modulator and polarized by a half and quarter wave plate pair. The telescope expands the beam so that it overfills the back aperture of the objective. The pair of galvanometric scanners raster scan the sample through a

scanning lens and the microscope objective. The back propagated portion of the fluorescence emitted by the sample is collected by the objective and passes through a dichroic mirror and projected onto a photomultiplier tube. The whole system is controlled by a computer that records the photons time of arrival and build fluorescence decay curves from the data [86].

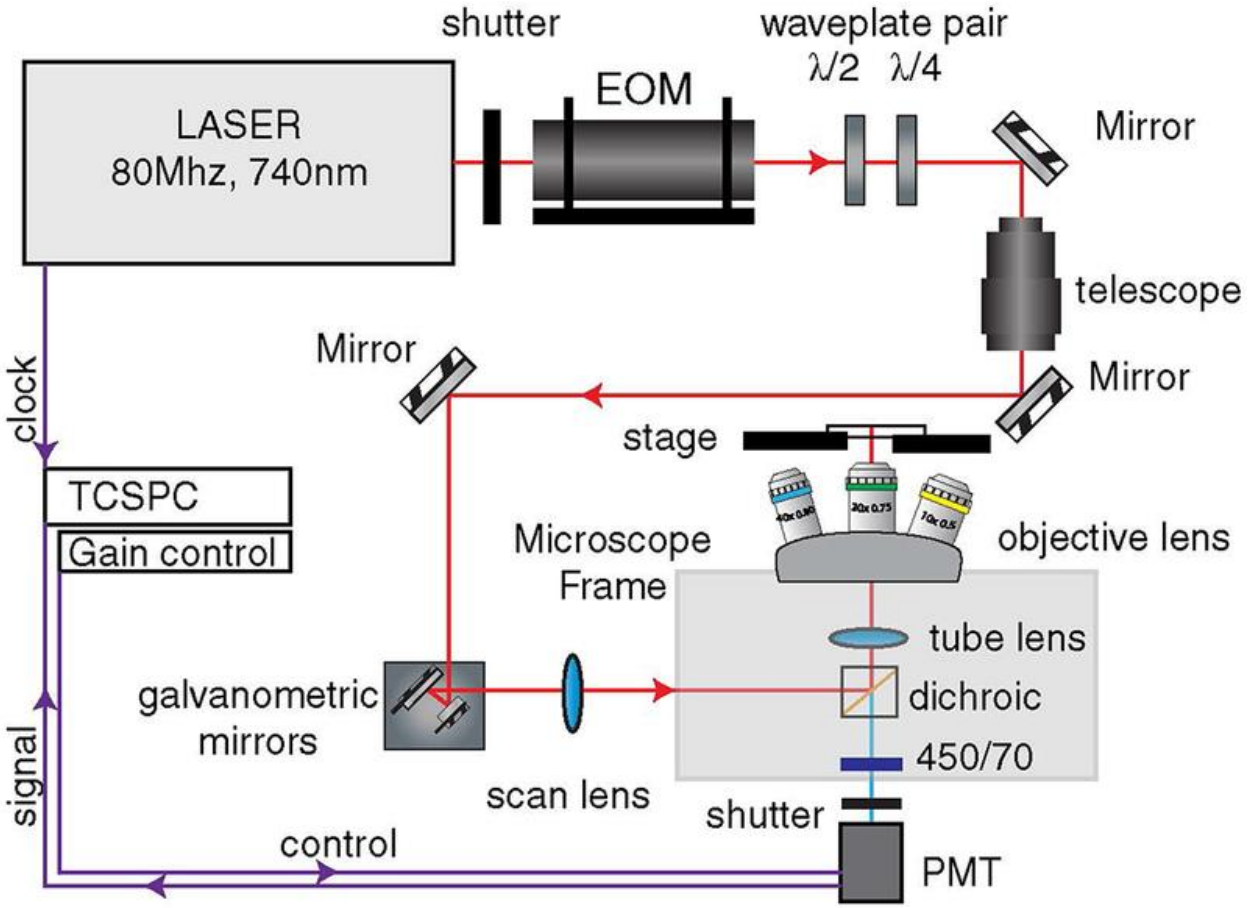

Figure 3.2. Schematic of the typical experimental setup for the multiphoton microscope used in the temporally resolved experiments. The microscope uses an ultrafast laser controlled for its power. It is equipped with multiple objective lenses, a Nikon 60× Fluo Oil objective was used for the experiments. Abbreviations used in the schematic are: TCSPC, time correlated single photon counting, PMT, photomultiplier tube, EOM, electro-optic modulator [87]. Figure adapted from Chacko, 2018.

Both multiphoton laser scanning acquisition systems were developed at LOCI: WiscScan is a laser scanning software package that combines nearly all the functionality of a laser scanning microscope apparatus into a single software package. The package performs waveform generation scanning, signal conditioning and microbeam pointing and runs inside of a commercial digital signal processor (DSP) residing on a peripheral component interconnect (PCI) card inside of a desktop. The program provides control for the microscopy focusing and stage movement through a graphical user interface (GUI) [88].

OpenScan is a customizable laser scanning microscopy (LSM) software platform that allows the user to set up basic LSM functionalities. This modular software package gives the user the ability to control the acquisition and on-board real time image processing and allows the user to fully customize all aspects of the hardware system such as timing signals and digital to analog conversion (DAC)/analog to digital conversion (ADC) control [89].

HEK293 cells were imaged using the 60× oil immersion lens (1.4 NA, Nikon, Melville, NY) with two-photon excitation set at 800nm and the emission signal was collected using a 480/40nm filter. The laser scanning interval for each image taken was 60s and the laser power at the sample was <8mW for the HEK293 cells. HEK293 cells were imaged for approximately an hour in 5% CO_2 at 35°C in a humidified environment using a live cell setup. The acquisition software 'WiscScan,' was coupled with galvanometric scanners to scan the sample with the laser, and the emission signal was collected using a high-gain photon counting GaAsP PMT (Hamamatsu, H7422P-40). The photon arrival times were calculated using Becker Hickl TCSPC electronics (SPC-150 board).

3.4 Two-photon fluorescence microspectroscopy

The OptiMiS^{TM} system developed by the Raicu Lab at the University of Wisconsin, Milwaukee and commercialized by Aurora Spectral Technology comprises of the components shown in figure 3.3 [90]:

1) Laser: Spectra-Physics MaiTai HP with wavelength range of 750nm – 1040nm
2) Detector: Andor iXon X3 electron multiplying CCD
3) Microscope: Nikon Eclipse Ti-E inverted microscope
4) Objective: 60× 1.4NA oil

The OptiMiS^{TM} system consists of a mode-locked laser that generates ultra-short pulses (100-fsec pulses) tuned to 800nm and 960nm. The excitation beam is focused onto the sample using an infinity corrected C-Apochromat, water immersion objective. The optical scanning head (used for beam scanning) was modified to incorporate a spatial light modulator (SLM) that was used for adaptive beam shaping. Using the SLM, a multibeam array is generated so that multiple voxels are scanned, concurrently. A non-descanned detection scheme is used to project the emitted fluorescence through a transmission grating and onto a cooled electron-multiplying charge coupled device (EMCCD) camera. This allows for the various wavelengths of light emitted by the sample to be separated into various wavelength channels. Software developed by the Raicu lab is used to control the SLM, optical scanning head and EMCCD camera [91].

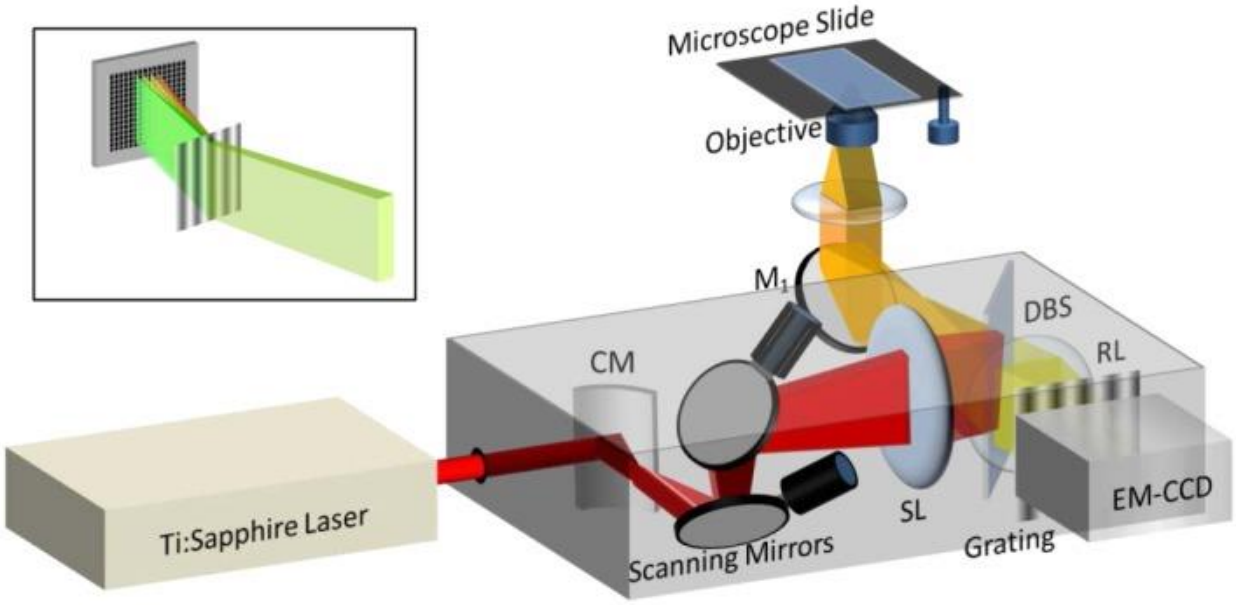

Figure 3.3 Schematic of OptiMiS Setup used in spectrally resolved experiments. The microspectroscope used for the spectrally resolved experiments is a multiphoton microscope with an ultra-fast laser. Abbreviations used are: <CM> cylindrical mirror, <SL> S- line Lens, <DBS> dynamic beam shaping, <RL> relay [92]. Figure adapted from Biener, 2014.

Fluorescence images of transfected cells were obtained using a spectrally resolved two-photon optical microspectroscope consisting of a tunable femtosecond laser (MaiTai, Spectra Physics, Santa Clara, CA), an inverted microscope (Nikon Eclipse Ti, Nikon Instruments Inc. Melville, NY) equipped with an infinity-corrected plan apochromat, oil immersion objective (60×, NA = 1.45; Nikon Instruments Inc.) and an OptiMis scanning/detection head (Aurora Spectral Technologies, Grafton, WI) [64].The system is controlled using software also developed by the Raicu lab for image acquisition. The transfected cells were scanned using a line-shaped excitation beam with an integration time of 35ms per pixel and a power of 300mW. Each field of view was scanned at two wavelengths, 800nm and 960 nm over a total time of ~60s. The output of each

excitation scan was set to microspectroscopic images, consisting of 200 different wavelength channels ~1nm bandwidth and the size of each emission image was 440×300 pixels.

3.5 Calculation of Apparent FRET Efficiency Using Temporal Resolution

The time-resolved fluorescence imaging data consisting of (x,y,t) information with each coordinate consisting of 265 data points was analyzed using SPCImage 8.7. SPCImage is a time-correlated Single Photon Counting Fluorescence Lifetime Imaging Microscopy (TCSPC-FLIM) data analysis software developed by Becker & Hickl GmbH that combines time-domain and frequency-domain analysis. It uses a maximum-likelihood algorithm to calculate the decay function in individual parameter. The program computes lifetime fits and amplitudes of the decay components and produces color- coded images of the amplitude and intensity weighted lifetimes in the pixels as well as many other functions [93].

Typically, images taken with temporal resolution seen in figure 3.4a undergo fluorescence lifetime imaging microscopy (FLIM) analysis which consists of fitting each decay curve as shown in figure 3.4b with either a single or two exponential curves as shown in figure 3.4c to give the lifetimes of the constructs/fluorescent molecules. With the tiFRET method, the fluorescence decay curve is numerically integrated instead (see fig 3.4d). The tiFRET method uses donor only fluorescence lifetime and the numerically integrated fluorescence decay curve to determine the apparent FRET efficiency for every pixel in the image stack.

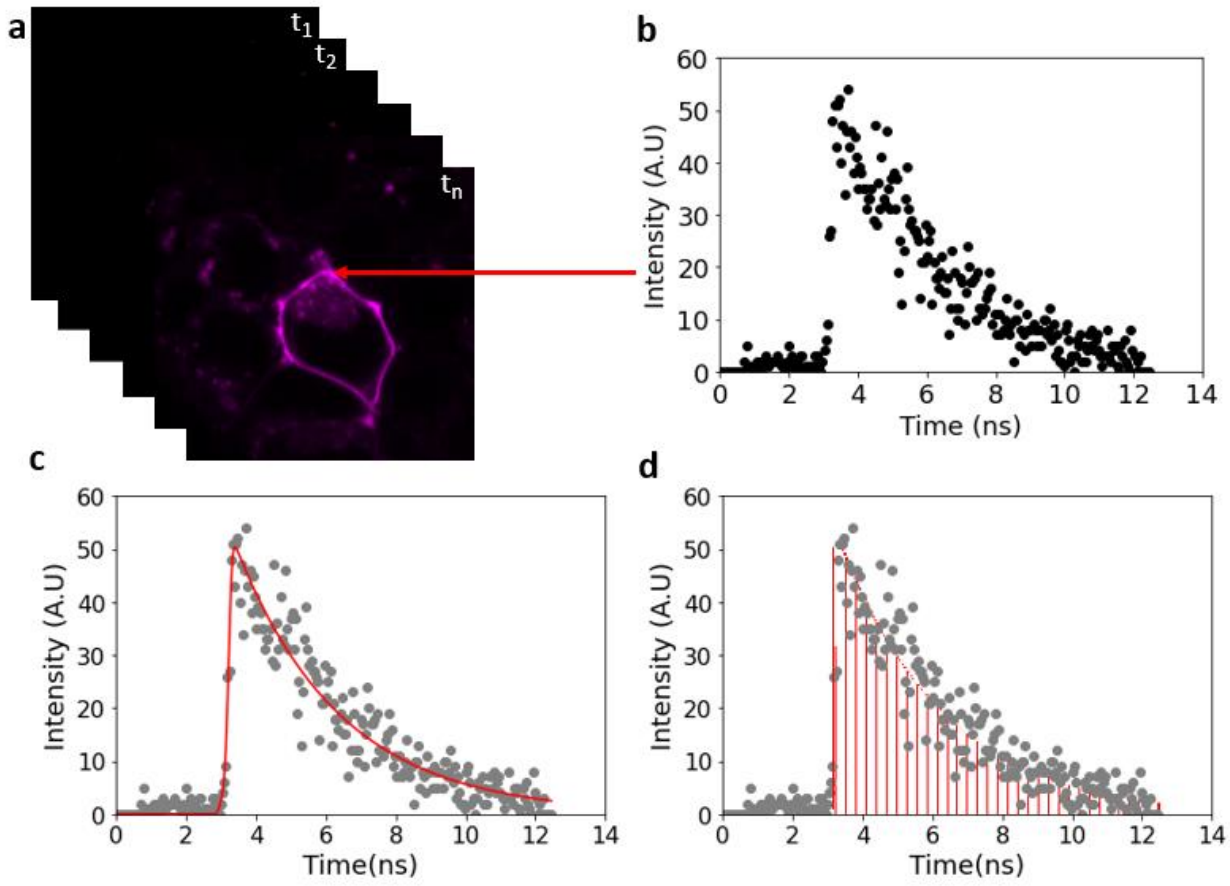

Figure 3.4 Illustration of the fluorescence decay curves from each pixel in the image with an exponential decay fit or integrated. (a) Image stacks made up of a photon micrograph at each time point was generated from the data (x, y, t) acquired. (b) Signal from each pixel depicts fluorescence decay curves. (c) Typically, in FLIM experiments, the fluorescence decay curves are fit with either a one or two exponential fits (one-lifetime fit is depicted) (d) For the temporally resolved experiments, numerical integration of the fluorescence decay curve was conducted.

In order to calculate the apparent FRET efficiency for each pixel in the fluorescence images, the donor only lifetime was needed. A single exponential fit of the donor only images, i.e., images containing cells expressing GFP_2 attached to M_2R only, was performed for each pixel-level decay curve and the lifetime decay values were exported to an ASC file as the one-lifetime images. The data files were used to construct a pixel level decay lifetime TIFF map using Python (Python

Software Foundation). An image stack of the one-lifetime images was generated as well as a stack of images containing the photon count only (intensity images).

Hand-drawn polygons surrounding the cell membranes (regions of interest (ROIS)) were made for each cell in each photon only as seen in fig 3.5a. A 10-pixel wide band inward from the drawn ROIs were generated and divided into segments, 200 pixels in area.

For each segment, histograms of frequency of peak vs. the fluorescence lifetime were generated and the two most prominent peaks were chosen as shown in fig 3.5b using a "goodness of fit" criterion. Peak candidates were selected by first determining the local maxima of the histogram and locating the nearest minima on the left and on the right of the curve. The standard error for each maximum was determined, and the amplitude of the peak computed as the difference between the maximum count and minimum count. If the maximum count value was at least 1 standard deviation greater than the minimum count value the peak was retained. This process was repeated for each peak in decreasing order, disregarding the peaks that did not fit the criteria. Ultimately, a metahistogram of the two most prominent peaks from each histogram vs. the fluorescence lifetime was generated. This metahistogram was then fitted with a single Gaussian curve with the peak value as the lifetime of the donor only (see fig 3.5c).

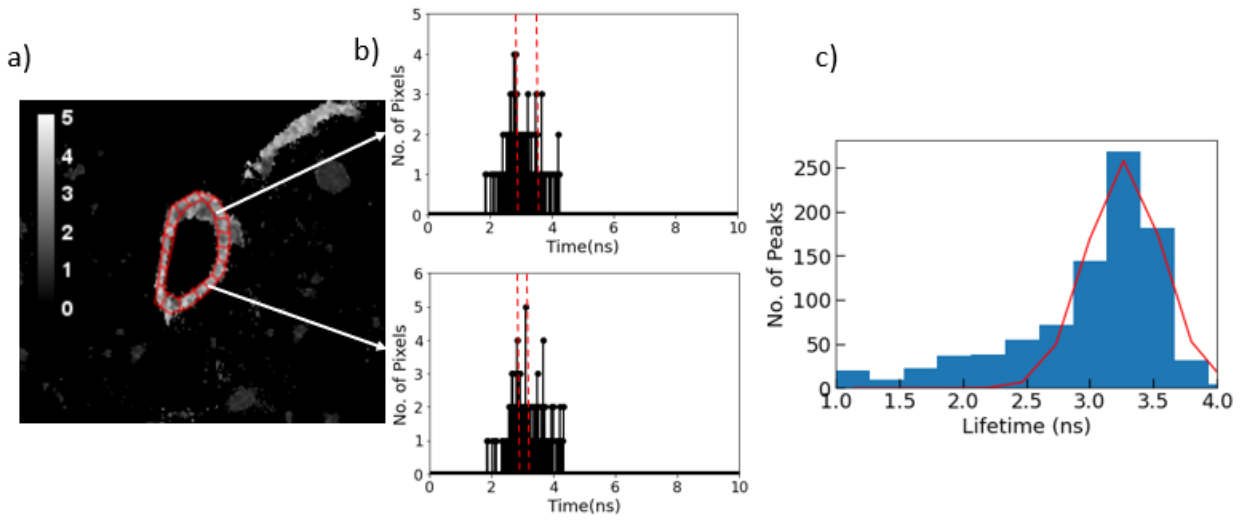

Figure 3.5 Experimental lifetime of the green fluorescent protein attached to M_2R. (a) Using SPCI image, image stacks for GFP_2 attached to M_2R were generated using the one-lifetime fit. The decay curve in each pixel was fit with a single exponential fit. (b) The ROI and segmentation process were applied to each image in the image stack, i.e., cell membrane ROIs were drawn for each cell in the image stacks and histograms of the number of pixel vs. the time were generated for each segment. (c) The metahistogram of number of peaks vs. the lifetime was fit with a single Gaussian. The mean of the Gaussian gives the fluorescence lifetime of the donor molecule in the absence of the acceptor.

Pixel level FRET efficiencies were obtained using the tiFRET method and the fluorescence lifetime of the donor. Raw images from SPCImage, i.e., images that had not been fitted or processed, were exported as ASC files. Using Python (Python Foundation Software), each ASC file was put through a program that numerically integrated each (x, y, t) coordinate in the image (p_{D*a}) and dividing by the amplitude of the fluorescence decay curve (p_{D*0}) and the fluorescence lifetime of the donor (τ_D) using the following equation in order to create image stacks of apparent FRET efficiency maps as shown in figure 3.6a. This method is based on applying the following equation to every pixel in the image stack to generate an apparent FRET efficiency map:

$$E_{app} = 1 - \frac{1}{\tau_D}\frac{\int_0^\infty p_{D*a}dt}{p_{D*0}}. \quad (3.1)$$

In order to sort the data, the fluorescence emission of the donor only (F_D) was calculated and image stacks of the fluorescence emission of the donor only were generated (see figure 3.6b). Using Python, the FRET efficiency was determined for each pixel using the aforementioned process and the fluorescence emission of the donor in the presence of the acceptor (F_{DA}) was determined by summing the photons in each pixel using the following equation [94, 95].

$$F_D = \frac{F_{DA}}{(1-E_{app})} \tag{3.2}$$

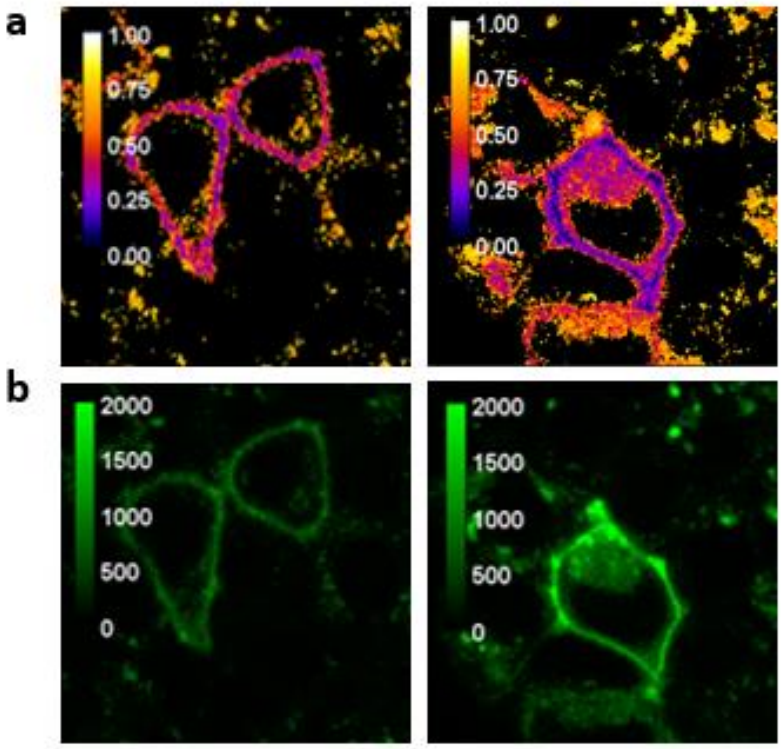

Figure 3.6 Generation of FRET and FD only maps. (a) Using equation 1, the FRET efficiency (E_{app}) distribution maps were generated from the raw images/unprocessed images taken using the temporally resolved experimental setup. (b) Fluorescence emission of the donor only in the presence of the acceptor (F_D only) image stacks were generated using equation 2.

In a process identical to the one outlined earlier in the determination of the fluorescence lifetime, using the intensity maps, stacks of images were generated with only the photon count so

that cell membrane ROIs and segments could be made. These ROIs and segments were mapped onto the apparent FRET efficiency maps and the Donor only map. Histograms of the frequency of the peaks vs. apparent FRET efficiency were generated and the two most visible peaks were selected. A metahistogram of the frequency of visible peaks vs. the apparent FRET efficiency was generated.

3.6 Calculation of apparent FRET efficiency using spectral resolution

In each microspectroscopic image, the measured emission spectrum for each pixel contains contributions from each fluorescent tag in the biological sample. To determine the apparent FRET efficiency, the spectra had to be unmixed. Images of M_2R attached to GFP_2 only and M_2R attached to YFP only were obtained using the OptiMiS setup described in the two-photon fluorescence microscopy section at two wavelengths 800nm and 960nm at 300mW. Elementary spectra of the donor only signal and acceptor only signal were generated from the M_2R attached to GFP_2 only and M_2R attached to YFP only respectively. Spectrally resolved images of HEK293 cells co-expressing M_2R attached to GFP_2 and YFP were obtained in an analogous fashion.

A single pixel in a two-dimensional fluorescence image contains a power spectrum from the emission of fluorescent molecules in that pixel. The measured power can be written as a combination of the power spectra of the individual fluorescent tags ($\mathbf{S_1, S_2, \dots S_l}$) multiplied by the coefficient proportional to the concentration of the fluorescent tag ($k_1, k_2, \dots k_l$) and can be written as equation 3.

$$\mathbf{P} = \bar{\bar{S}}.\,k + n \qquad (3.3)$$

P is the measured intensity spectrum vector for m wavelength channels and n is the experimental noise term from either external or camera noise. $\bar{\bar{S}} = \mathbf{[S_1, S_2, \dots S_m]}$ is the $m \times l$ matrix

of l individual spectra of fluorescent tags with m measured wavelength channels and k is the vector of coefficients $\mathbf{k} = [k_1, k_2, \ldots k_l]$ [96].

A least squares minimization procedure was used to extract the k vector in order to determine the number of fluorescent molecules within a particular pixel for each fluorescent tag as seen in equation 4 [96].

$$\mathrm{Min}_k \|\mathbf{P} - \bar{\bar{S}}.\, k\|_2^2 \tag{3.4}$$

Taking a derivative of equation 4 to be minimized to k equal to zero and rearranging give the equation 5 for k. T is the transpose of the matrix [96].

$$\mathbf{K} = (\bar{\bar{S}}^{\mathbf{T}}.\, \bar{S})^{-1}.\, \bar{\bar{S}}^{\mathbf{T}}.\mathbf{P} \tag{3.5}$$

Both S and P are measured quantities. $\bar{\bar{S}}$ was measured by imaging the individual fluorescence spectra of each species i.e. M_2R attached to GFP_2 only (S_D, the elementary donor power spectrum) and M_2R attached to YFP only (S_A, the elementary donor power spectrum) and each sample was normalized to its maximum. P is the pixel power spectrum along m channels [96].

The background spectrum is included to reduce the pixel non-uniformity of the measuring system. The spectral images of cells co-expressing M_2R attached to GFP_2 and M_2R attached to YFP were unmixed using the above procedure using S_D and S_A to obtain separate donor (k^{DA}) and acceptor (k^{AD}) images[96].

$$E_{app} = \frac{1}{\left[1+\frac{Q^A w^D k^{DA}}{Q^D w^A k^{AD}}\right]} \tag{3.6}$$

The apparent FRET efficiency (E_{app}) distribution of an image cell is calculated using the spatial intensity maps separated for donor and acceptor signals (k^{DA} and k^{AD}), the integrals of the measured elementary spectra (w^D and w^A), and the quantum yields of the donor and acceptor (Q^D =0.55 and Q^A = 0.61) assuming negligible direct excitation of the acceptor fluorophore [96].

The spectral unmixing was done using OptiMiS DC, a program developed by the Raicu Lab using MatLab (MathWorks Inc., USA). From the unmixed images, the apparent FRET efficiency maps were obtained with various signal to noise threshold applied. Pixels showing only background noise were avoided by setting $E_{app} = 0$ for the pixel characterized by a signal to noise ratio of less than one standard deviation of the noise for both donor and acceptor signals.

ROIs of the cell membrane were hand drawn along the cell membranes in the spectrally unmixed images and the segmentation process was applied with a 10-pixel band and the 200-pixel area segments. This process was identical to the ROI and segmentation process described in the determination of donor lifetime section.

3.7 Analysis of Metahistograms using Parallelogram Shaped Tetramer Model

Metahistograms from the temporally resolved and spectrally resolved experiments were analyzed identically. Using the kinetic based theory of FRET, the average FRET efficiency per donor can be calculated for an oligomer size n, containing k donors, and n-k acceptors. The FRET efficiency of i^{th} donor of configuration q with k donors can be written in terms of the pairwise FRET efficiency, E_p and the distances between the complexes, r [97].

$$E_{i,j,k} = \frac{E_p \sum_j (\frac{r_1}{r_{ij}})^6}{1 - E_p + E_p[\sum_j (\frac{r_1}{r_{ij}})^6]} \quad (3.7)$$

The variables r_1 and r_{ij} represent the distance that corresponds to the pairwise FRET efficiency, E_p, and the distance between the i^{th} donor and j^{th} acceptor, respectively.

A parallelogram shaped tetramer model was used to fit the metahistogram data. The FRET efficiency of each configuration was calculated using equation 7. Three geometric variables: the pairwise FRET efficiency, E_p, the ratio between the distances of the oligomer, r_1/r_2 and the acute

angle of the parallelogram, α as shown in figure 3.7 were varied in order to determine the FRET efficiency of the parallelogram shaped tetramer model.

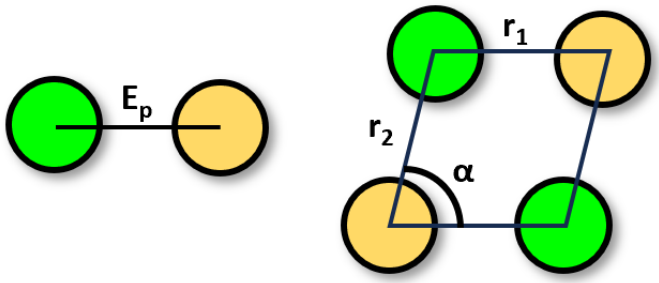

Figure 3.7 Schematic of the parallelogram shaped tetramer used for the fitting model and the description of the geometric variables. The pairwise FRET efficiency (E_p) is the efficiency of energy transfer between a donor and acceptor molecule at distance r_1. The ratio of the distances gives r_1/r_2 and the acute angle of the parallelogram is α.

Seven Gaussians were generated each with its own FRET efficiency (see Table 3.1) at the mean of the Gaussian determined by the three geometric variables. The amplitudes and widths (i.e., standard deviations) of the Gaussians were allowed to vary along with the three geometric variables as the fitting parameters of the model. The theoretical fit was calculated by summing each of the Gaussians from the models.

The fitting residual was calculated using equation 8 for the theoretical curve in relation to the data points of the metahistogram. The fitting parameters of the model were varied to ensure the lowest fitting residual for each metahistogram was obtained.

$$\text{Res} = \sqrt{\sum(\text{Data} - \text{ModelFunction})^2} \tag{3.8}$$

Table 3.1 FRET efficiencies corresponding to each donor-acceptor configuration for the parallelogram shaped tetramer model. In the left column, a schematic representation of the donors (green) and acceptor (yellow) ratios in each configuration. The middle column denotes the Gaussian associated with the configuration. The right column shows the calculated apparent FRET efficiency of the tetramer for the parallelogram shaped model.

Configuration	q	FRET Efficiency
	1	$\frac{1}{3}\left[E_p + \frac{E_p(\frac{r_1}{r_2})^6}{1 - E_p + E_p(\frac{r_1}{r_2})^6} + \frac{E_p(\frac{r_1}{r_{d2}})^6}{1 - E_p + E_p(\frac{r_1}{r_{d2}})^6}\right]$
	2	$\frac{1}{3}\left[E_p + \frac{E_p(\frac{r_1}{r_2})^6}{1 - E_p + E_p(\frac{r_1}{r_2})^6} + \frac{E_p(\frac{r_1}{r_{d1}})^6}{1 - E_p + E_p(\frac{r_1}{r_{d1}})^6}\right]$
	3	$\frac{1}{2}\left[\frac{E_p((\frac{r_1}{r_2})^6 + (\frac{r_1}{r_{d1}})^6)}{1 - E_p + E_p((\frac{r_1}{r_2})^6 + (\frac{r_1}{r_{d1}})^6)} + \frac{E_p((\frac{r_1}{r_2})^6 + (\frac{r_1}{r_{d2}})^6)}{1 - E_p + E_p((\frac{r_1}{r_2})^6 + (\frac{r_1}{r_{d2}})^6)}\right]$
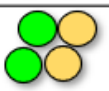	4	$\frac{1}{2}\left[\frac{E_p + E_p(\frac{r_1}{r_{d1}})^6}{1 - E_p + E_p(1 + (\frac{r_1}{r_{d1}})^6)} + \frac{E_p + E_p(\frac{r_1}{r_{d2}})^6}{1 - E_p + E_p(1 + (\frac{r_1}{r_{d2}})^6)}\right]$
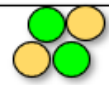	5	$\frac{E_p + E_p(\frac{r_1}{r_2})^6}{1 - E_p + E_p(1 + (\frac{r_1}{r_2})^6)}$
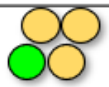	6	$\frac{E_p(1 + (\frac{r_1}{r_2})^6 + (\frac{r_1}{r_{d2}})^6)}{1 - E_p + E_p(1 + (\frac{r_1}{r_2})^6 + (\frac{r_1}{r_{d2}})^6)}$
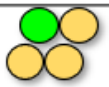	7	$\frac{E_p(1 + (\frac{r_1}{r_2})^6 + (\frac{r_1}{r_{d1}})^6)}{1 - E_p + E_p(1 + (\frac{r_1}{r_2})^6 + (\frac{r_1}{r_{d1}})^6)}$

In order to fit the data with a theoretical model, automatic fitting procedures were implemented. However, due to the number of steps constraints and initial conditions, the residual for the fit could often be stuck in a local minimum. To avoid this, an iterative fitting procedure was implemented by varying the value of r_1/r_2 within a specified range for a single value of alpha and pairwise FRET efficiency within specified ranges. The fitting residual was calculated for each

automatic fit and a three-dimensional cube of the geometric variables was plotted, the fourth variable, the fitting residual was assigned a color to provide a four-dimensional representation of the data being fit to the theoretical models as shown in fig 3.8. The data was then sorted based from highest to lowest fitting residuals and the geometric and statistical variables (the amplitudes and standard deviations of each Gaussian) of each fit were obtained.

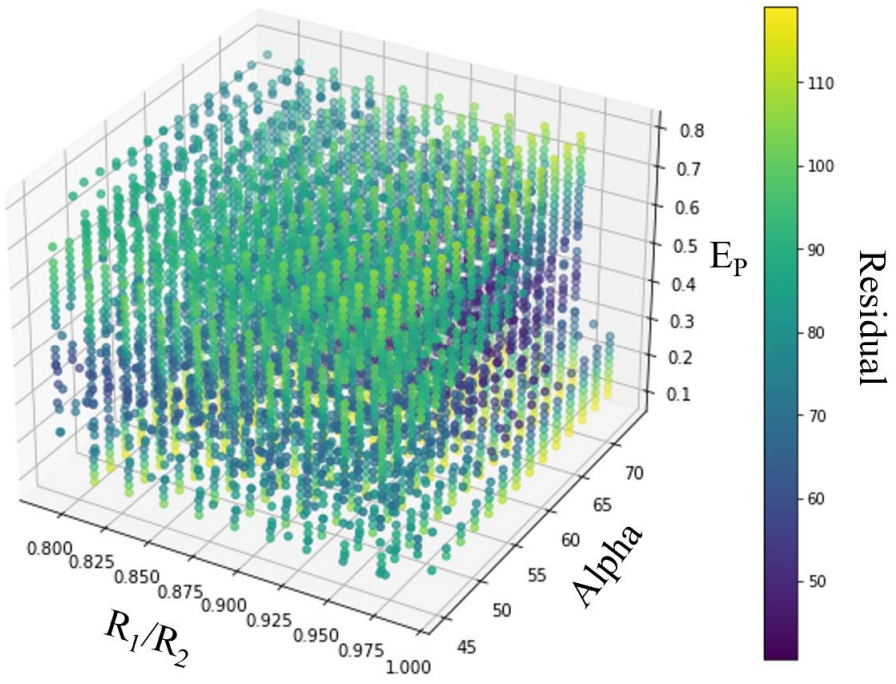

Figure 3.8 Typical diagram depicting the automatic iterative fitting procedure of the geometric model applied to the FRET efficiency metahistograms. The experimental data was fitted automatically using the least square algorithm by fixing two of the geometric variables and iteratively varying the third to span the full range of r_1/r_2, alpha and E_p values to find the global minimum for the fitting residuals.

Each of the best fit parameters was used as the set of initial conditions for manual refinement. Once the fits were manually refined, a single Gaussian of fixed mean, amplitude and standard deviation was placed at one of the unfit peaks of the metahistograms. The program was

allowed to automatically refine the fit once more to obtain the lowest fitting residual. The process was repeated once more for a total of two fits with a fixed peak. The geometric variables from the best fits were obtained.

The dimensions of the oligomer were determined from the three geometric variables. For a parallelogram shaped tetramer, the sides of the oligomer were calculated as follows: r_1 was obtained from the equation

$$r_1 = R_0 \left(\frac{1-E_p}{E_p}\right)^{\frac{1}{6}}, \tag{3.9}$$

and r_2 was obtained from the ratio, r_1/r_2. The diagonal distances were calculated using the trigonometric equations

$$r_{d1}^2 = r_1^2 + r_2^2 + 2r_1 r_2 \cos\alpha, \tag{3.10}$$

$$r_{d2}^2 = r_1^2 + r_2^2 - 2r_1 r_2 \cos. \tag{3.11}$$

R_0 is the Förster distance, defined by eqn. 2.2 above, and which is dependent on the FRET pair. For GFP_2 and YFP, the Förster distance is 57Å [58]. R_1 is the distance between the molecules that correspond to the pairwise FRET efficiency, i.e., the width of the parallelogram and r_2 is the length of the parallelogram as shown in figure 3.7. The diagonal distances are represented by r_{d1} and r_{d2}.

Chapter 4

RESULTS

Fluorescence lifetime imaging microscopy (FLIM) is a well-established technique that uses the characteristic fluorescence lifetime of molecules to perform non-destructive measurements on biological systems. This technique has is highly sensitive to the molecular environment and changes in molecular conformation and has been used in a number of studies for auto-fluorescent molecular imaging, protein-protein interactions and monitoring numerous processes in cell and tissues [67]. FLIM extracts fluorescent molecules lifetimes by fitting image pixel-level fluorescence decay curves with exponentials. FLIM is often used to perform FRET measurements to study protein-protein interactions for bi-molecular interactions [98]. However, a priori knowledge of the sizes of the oligomer is required in order to successfully use the method, since it is directly related to the number of exponentials used to fit the fluorescence decay curves. To address this limitation, our lab has recently developed a method dubbed time-integrated FRET (tiFRET) [99].

tiFRET circumvents the limitation of prior knowledge of the oligomer size by numerically integrating the fluorescence decay curves as opposed to the traditional method of fitting with one or two exponential fits to determine the lifetime. Generally, when using FLIM, the FRET efficiency of the system is calculated using the following equation,

$$E = 1 - \frac{\tau^{DA}}{\tau^{D}}, \tag{4.1}$$

where τ^{DA} is the lifetime of the donor molecule in the presence of the acceptor obtained from the exponential fit of the fluorescence decay curves from images of systems containing both donor and acceptor molecules, and $\tau^{D}$is the lifetime of the donor only molecule obtained from

exponential fit of the fluorescence decay curves obtained from images of the donor only molecules [99].

However, this equation does not take into account approximations that are often used in FRET studies such as direct excitation of the acceptor. [100] Another limitation of this FLIM-FRET method is the accuracy to which the fluorescence lifetimes can be determined. Extracting more than two lifetimes is difficult and restricts the number of molecules that the method can be applied to, to two.

By numerically integrating over the fluorescence decay curve of the donor in the presence of the acceptors (p_{D*a}) over the time interval between two excitation pulses and dividing by the amplitude of the fluorescence decay curve (p_{D*0}), the apparent FRET efficiency can be determined without knowing the size of the oligomer using the following equation [100]

$$E = 1 - \frac{1}{\tau^D}\frac{\int_0^\infty p_{D*a}dt}{p_{D*0}} \tag{4.2}$$

The viability of the method was originally tested using cytoplasmic constructs of predetermined size. A comparison between traditional one and two lifetime fits and the tiFRET method was conducted to determine the FRET efficiencies of three cytoplasmic constructs of Cerulean (donor, D), Venus (acceptor, A) and Amber (non-fluorescent, N) in the forms I, NDA and ADA. The weighted averages and the standard deviations of the FRET efficiencies of the constructs were compared to each other to assess the performance of the tiFRET method.

HEK 293 cells transiently transfected with plasmids containing DNA that expressed human muscarinic receptors, M_2R, fused to either the green fluorescent protein GFP_2 [58], which was used as a donor, or the yellow fluorescent protein YFP [41, 101], used as an acceptor. The donor- and acceptor-tagged M_2R have been either transfected singly or in combination with the co-transfection

ratios of 1:1 and 1:3 donor to acceptor. The donor only tagged M_2R was used to collect the donor spectrum for the spectrally resolved experiments and the donor only lifetime for the temporally resolved experiments, the acceptor only tagged M_2R was used to collect the acceptor spectrum for the spectrally resolved experiments. The donor only lifetime was used to calculate the pixel level FRET efficiency using the tiFRET method as described in Chapter 3, Methods section 3.5 Calculation of Apparent FRET Efficiency Using Temporal Resolution. The donor and acceptor spectra were used for pixel level unmixing and calculation of FRET efficiency as shown in Chapter 3, Methods 3.6 Calculation of Apparent FRET Efficiency Using Spectral Resolution.

Temporally resolved fluorescence measurements were conducted using a multiphoton microscope time-resolved (see Chapter 3, Methods section 3.3 for details on the microscope), and images, with fluorescence decay curves in each pixel were obtained. For comparison, spectrally resolved experiments using two photon fluorescence microscopy were conducted using the same biological system where images with high spatial resolution were obtained [53]. The results of each experiment type were analyzed in according to the methods outlined in Chapter 3, Methods sections 3.5 for the temporally resolved experiments, 3.6 for the spectrally resolved experiments and 3.7 for both, to determine the configuration and geometry of the oligomers. In this chapter, the results and analysis of both types of experiments are presented.

4.1 Determining the fluorescence lifetime of the donor

Fluorescence micrographs of cells expressing M_2R fused to GFP_2 only were obtained using the custom multiphoton microscope controlled using the OpenScan and WiscScan software from LOCI located at the University of Wisconsin, Madison [87]. Using SPCImage (Single Photon Counting Image) software developed by Becker and Hickl [93], a single exponential fit was

applied to fluorescence lifetime decay curves in each pixel in order to obtain the fluorescence lifetime of the donor only.

Hand-drawn polygons surrounding the outer side of the cell membranes, also known as regions of interest (ROIs), were made for each cell in the micrographs using an image stack of the intensities, and further divided into sections of 200 pixels in area, 10 pixels in width from the inner edge of the ROIS, these sections are called segments and are shown in Figure 4.1a. The ROIs and segments were then mapped onto the one lifetime image stack, and histograms of the number of pixels vs. lifetime were generated for each segment (see figure 4.1b). The two most common lifetime values, i.e., the two more visible peaks in the histogram of the no of pixels vs. time were then extracted from each segment histogram. Figure 4.1c shows the metahistogram of the frequency of peaks vs. the lifetime, that was obtained and fit with a single Gaussian, the peak of which gives the fluorescence lifetime of the donor, τ^D =2.63ns for M_2R-GFP_2.

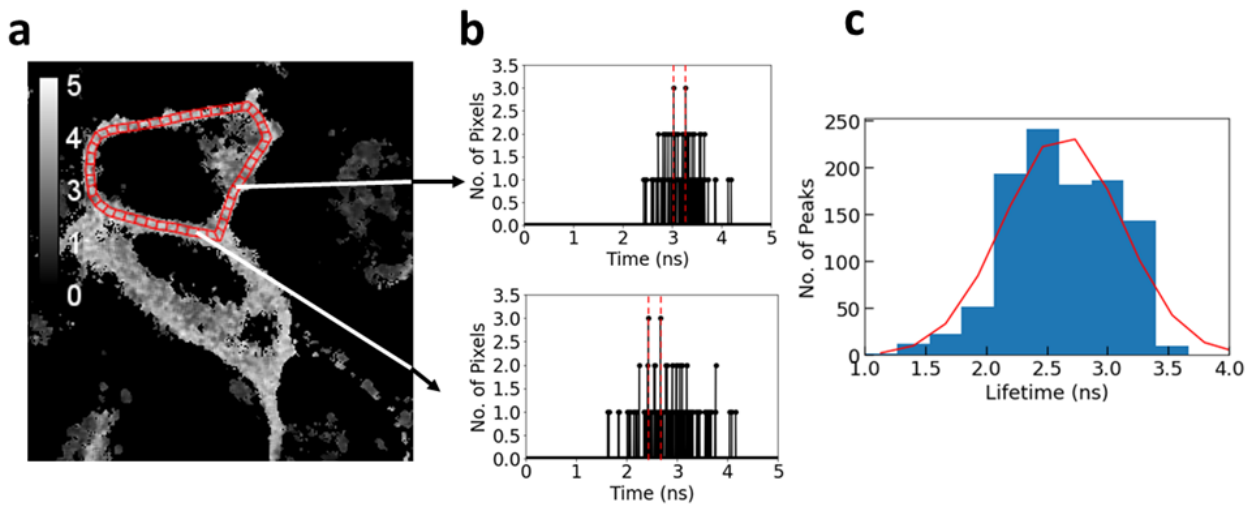

Figure 4.1. Experimental lifetime of green fluorescent protein attached to the human muscarinic receptor 2. (a) Image stacks for the GFP_2 attached to the M2 receptor data were generated using the one lifetime fit. The lifetime from each pixel determined from the exponential fit of the fluorescence decay curves. Hand drawn polygons surrounding the outer edge of the membrane called ROIs were drawn for each cell. Segmentation, the process of generating a band 10 pixels inward from the ROI and dividing it into sections 200 pixels in area, was applied to every ROI. **(b)** Histograms of the no of pixels containing a particular fluorescence lifetime were generated for each segment and the two most prominent peaks for each histogram was obtained. **(c)** From each histogram, the two most prominent peaks corresponding to the most commonly occurring fluorescence lifetime values were chosen and a metahistogram of the most prominent peaks from each histogram vs. the lifetimes was generated. The metahistogram was fit with a single Gaussian. The mean of the Gaussian was the fluorescence lifetime of the donor only. The fluorescence lifetime of the donor molecule was found to be 2.63ns.

4.2 Obtaining E_{app} and F_D only maps for the temporally resolved experiments

Using the donor only fluorescence lifetime, determined using the modification of the standard FLIM method, the apparent FRET efficiency was calculated for each pixel in the stack of

temporally resolved images for the co-transfected ratios of M_2R attached to GFP_2 and YFP and E_{app} maps were generated as described in Chapter 3 section 3.5.

Using intensity image stacks for the co-transfected ratios of M_2R fused to GFP_2 and M_2R fused to YFP, each fluorescence decay curve in each pixel was numerically integrated over the time interval between two pulses, the apparent FRET efficiency (E_{app}) of each pixel was calculated using equation 2 and apparent FRET efficiency maps were generated. From the apparent FRET efficiency maps and the intensity image stacks, the fluorescence emission from the donor in the presence of the acceptor (F_D only) was calculated for each pixel and F_D only maps were generated as described in Chapter 3 section 3.5, the E_{app} and F_D only maps are shown in Figure 4.2.

Cell membrane ROIs were drawn on to the intensity image stack and the segmentation, process was applied, described in the previous section, to obtain a first set of segments 200 pixels in area, represented by the cyan segments in figure 4.2. Once the segmentation process was complete, new segments were generated by rotating the segments by a number of pixels to sample another region, represented by the red segments in figure 4.2, in an attempt to reduce noise in a process called resegmentation.

These ROIs and segments were then mapped on to the E_{app} and F_D only maps. In order to determine the quaternary structure of the M_2R oligomers, large numbers of cell level histograms were obtained of the apparent FRET efficiency values for each segmented and re-segmented area and the two most prominent peaks from each histogram were extracted. The donor only concentration was obtained in a similar fashion from the F_D only maps in order to sort the segment level E_{app} histograms and assemble the metahistogram, to ensure low donor concentration.

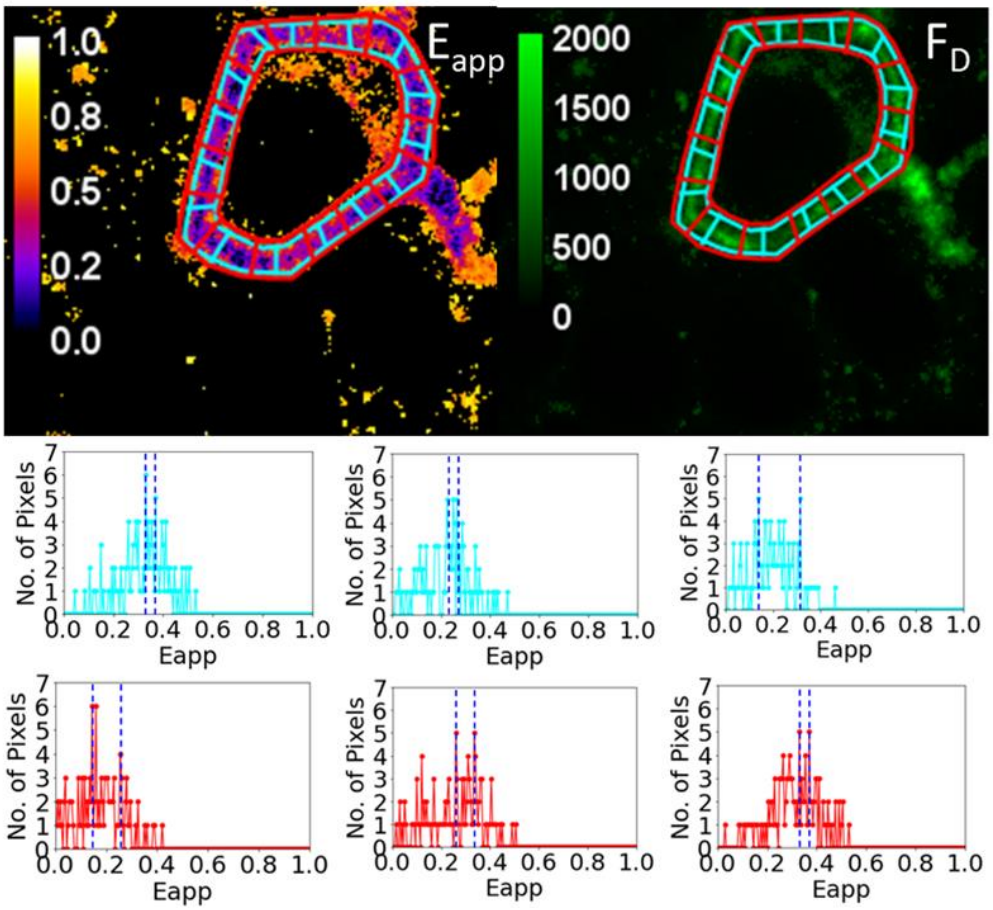

Figure 4.2. Illustration of the FRET efficiency distribution map and F_D only map. Using equation 1, the FRET efficiency distribution maps (E_{app}) can be generated from the image stacks. A map of the fluorescence emission from the donor only was generated using a similar method. First, the intensity in each image in the stack was summed to find the total intensity in each pixel. The resulting intensity was the fluorescence emission of the donor in the presence of the acceptor (F_{DA}). The donor only fluorescence emission (F_D) was subsequently calculated using the equation 2. The ROI and segmentation process was applied to the FRET distribution maps, and a histogram for each pixel was generated. From each histogram, the two most prominent peaks were obtained.

4.3 Obtaining E_{app} and F_D only maps for the spectrally resolved experiments

The results of the temporally resolved method to conduct FRET spectrometry experiments were compared to the well-established spectrally resolved method of conducting FRET spectrometry

wherein the FRET efficiencies at pixel level are determined from spectrally resolved measurements. Using the cells expressing M_2R fused to GFP_2 only and the M_2R fused to YFP only, the donor spectrum and the acceptor spectrum were obtained. Fluorescence micrographs of cells co-expressing M_2R fused with GFP_2 and M_2R fused with YFP in ratios 1:1 and 1:3 were obtained using the optical microscopy setup (OptiMiS) developed by the Raicu lab [102]. The images were unmixed using a pixel level unmixing algorithm in order to obtain apparent FRET efficiency and spatial intensity maps of the donor in the presence of the acceptor [64] using the procedure described in Chapter 3, Methods, section 3.6.

Apparent FRET efficiency maps and fluorescence emission of the donor in the presence of the acceptor were generated as outlined in Chapter 3, Methods, section 3.6. The procedure for obtaining ROIs, segmentation and resegmentation were identical to that of the temporally resolved. Cell membrane ROIs were mapped onto the E_{app} and F_D only and the segmentation and re-segmentation processes were applied. The process of extracting histograms and subsequent metahistograms from the data was identical to the aforementioned processes.

4.4 Generating Metahistograms

Metahistograms assembled from the temporally resolved and spectrally resolved data were fit with a parallelogram shaped quaternary structure model that was used to extract geometric parameters. Using the kinetic theory of FRET [100], the average FRET efficiency per donor can be calculated for an oligomeric complex of size ,n, that contains k donors and n-k acceptors of configuration, q. The FRET efficiency of the ith donor in the complex can be written in terms of the pairwise FRET efficiency.

$$E_{i,k,q} = \frac{E_p \sum_j (\frac{r_1}{r_{ij}})^6}{1 - E_p + E_p \sum_j (\frac{r_1}{r_{ij}})^6} \quad (3)$$

E_p is the pairwise FRET efficiency, r_1 is the one of the distances in the complex that corresponds to the pairwise FRET efficiency [96]. The average efficiency per donor is calculated using the following equation

$$E_{k,q} = \frac{1}{k} \sum_i E_{i,k,q} \quad (4)$$

For a specific oligomeric model containing n protomer, $E_{k,q}$ for each k and q. These $E_{k,q}$ values correspond to the predominant peak positions in the metahistogram. The metahistogram was fit using a model consisting of Gaussians with peak positions occurring at $E_{k,q}$. The simulated curve of the fitting model consists of the sum of Gaussians and is represented the following equation[96]

$$M(E_{app}) = \sum_q A_q \exp\left[-\frac{(E_{app} - E_{k,q})^2}{2\sigma_q^2}\right] \quad (5)$$

A_q represents the amplitude of the qth Gaussian distribution and σ_q is the standard. For degenerate FRET efficiency, a single FRET efficiency was used.

The model predicted a number of Gaussian peaks whose relative positions were determined by the geometrical parameters: the pairwise FRET efficiency E_p, the ratio of the side lengths of the oligomer r_1/r_2, and the acute angle between the sides α. This model resulted in a total of seven Gaussian peaks dependent on the geometrical parameters and the donor to acceptor ratio (See fig 4.4c) summed to provide an overall theoretical fit. The peak positions of the Gaussians were calculated using the kinetic theory of FRET [97, 100] as described in the Chapter 3, Methods section 3.7. Additionally, the theoretical curves were dependent on the amplitudes and standard deviations of the Gaussians where the amplitudes corresponded directly to the frequency of occurrence of the peaks. The difference between the experimental data and the theoretical fit was calculated in order to determine the fitting residual of the theoretical model, see Chapter 3,

Methods, section 3.7. The lower the residual, the closer the theoretical fit is to the experimental data suggesting that the model is accurate.

To ensure that the lowest residual for the automatic fit was a global minimum and not a local minimum, an iterative process of varying the three geometric variables and automatically fitting the data using a least square algorithm to determine the lowest fitting residual was applied to the temporally resolved and spectrally resolved metahistograms.

4.5 Automatic Iterative Fitting Procedure

In order to fit the data with a theoretical model, automatic fitting procedures were implemented. However, due to the number of steps constraints and initial conditions, the residual for the fit could often be stuck in a local minimum. To avoid this, an iterative fitting procedure was implemented by varying the value of r_1/r_2 within a specified range for a single value of alpha and pairwise FRET efficiency also within specified ranges. The fitting residual was calculated for each automatic fit and a three-dimensional cube of the geometric variables was plotted. The fourth variable, the fitting residual was assigned a color to provide a four-dimensional representation of the data being fit to the theoretical models. The data was then sorted based in order of highest to lowest fitting residuals and the geometric and statistical variables (the amplitudes and standard deviations of each Gaussian) were obtained. For further refinement, the three lowest fitting residuals, the best fits, and the corresponding geometric and statical variables were used as initial conditions.

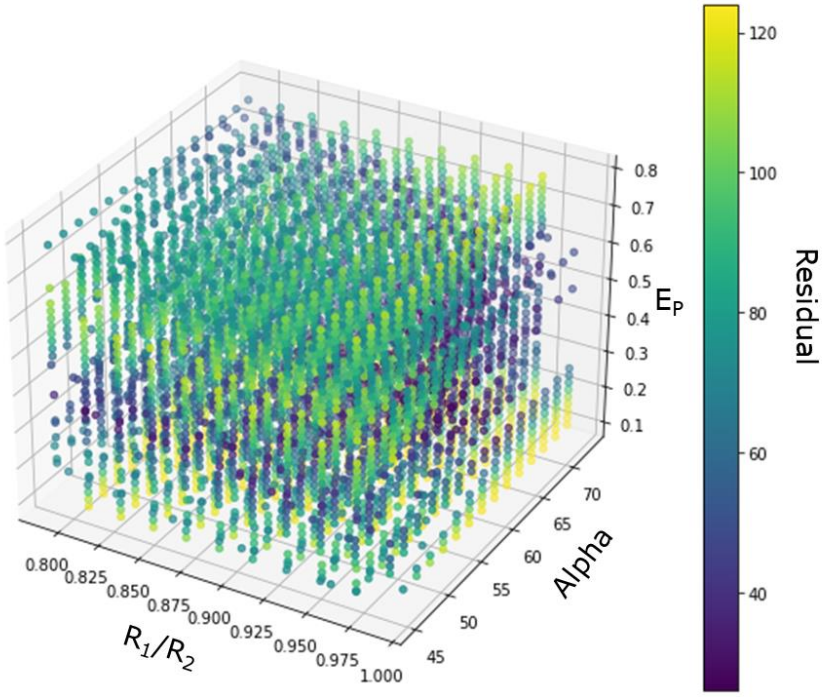

Figure 4.3. Four-dimensional representation of the iterative process of lowering the fitting residual. The experimental data was fitted automatically by fixing two of the geometric variables and iteratively varying the third to span the full range of r_1/r_2, α, and E_p values to find the global minimum for the fitting residuals.

4.6 Metahistogram Fitting with Substates

Previously, FRET spectrometry experiments have been limited to the average or most probable quaternary structure [77, 103] instead of a more dynamic structure. However, both experimental methods such as fluorescence spectroscopy and computer-based methods such as molecular dynamic simulations have shown that the tertiary structure of GPCRs are not rigid but are rather dynamic in nature and can switch between multiple conformational substates [64, 104-107]. It can be expected that these fluctuations in tertiary structure can also lead to variety in the quaternary structure substates [64]. These substates are conformational quaternary structural fluctuations that can lead to variations in the apparent FRET efficiencies and lead to peaks that are not typically captured by the model.

After the automatic iterative fitting procedure, the three best fits were manually refined using the geometric and statistical variables as the initial conditions. The variables were adjusted to visually improve the fit and lower the residual. From there a Gaussian was fixed at a specific FRET efficiency value, standard deviation and amplitude, to capture a peak value in the data that may have been originally ignored by the initial automatic and manual fits. An automatic fitting algorithm using the least squares algorithm was then applied to the manually refined fit of the metahistograms containing the fixed Gaussian in order to obtain the geometric variables for the lowest residual. This fixed Gaussian was representative of possible substates that exist within the oligomers or higher order oligomers that would not be captured with the tetrameric model. This process was done for both the temporally resolved and spectrally resolved data as shown in figures 2a and 2b.

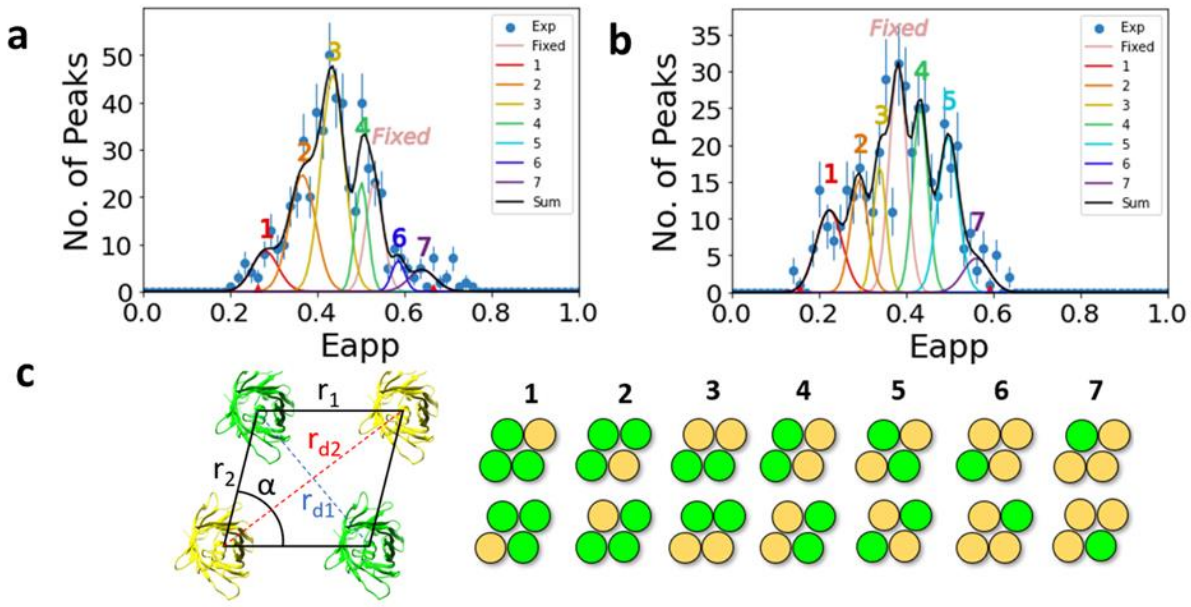

Figure 4.4. Illustration of the fitted metahistogram for the human muscarinic receptor 2 with fluorescent proteins attached. Using the FRET distribution map, regions of interest were drawn and segmented with a membrane thickness of 10 pixels and 200 x 200 pixels per segment. The FRET efficiencies from each pixel in the segment were obtained. Histograms of the frequency of the FRET efficiencies in each segment were generated. The geometric variables used in the fitting were the pairwise FRET efficiency (E_p), the ratio between r_1 and r_2 (r_1/r_2) and the acute angle between them (α). **(a)** Metahistogram obtained from temporally resolved data and fitted using the rhombic tetramer model. The best-fit parameters of the model were: $E_p = 0.448$, $r_1/r_2 = 0.945$, $\alpha = 66.1$. **(b)** Metahistogram obtained from spectrally resolved data and fitted using the rhombic tetramer model. The best-fit parameters were: $E_p = 0.382$, $r_1/r_2 = 0.918$, $\alpha = 65.4$. **(c)** The metahistogram was fitted using a rhombic tetramer model. The dimensions of the parallelogram is given, r_1 and r_2 represent the width and length of the tetramer. Similarly, r_{d1} and r_{d2} represent the diagonal lengths of the parallelogram shaped tetramer. Each Gaussian represents one configuration of the rhombic tetramer that was calculated using the geometric variables.

The geometric variables of the temporally resolved and spectrally resolved were obtained from the fits of the metahistograms as shown in table 4.1. For the temporally resolved experiments, the geometric variables were found to be: $E_p = 0.448$, $r_1/r_2 = 0.945$, $\alpha = 66.1$. For the spectrally

resolved experiments, the geometric variables were found to be: $E_p = 0.382$, $r_1/r_2 = 0.918$, $\alpha = 65.4$. Both fits were obtained using a tetrameric model with an additional fixed Gaussian.

Table 4.1. Best-Fit Geometric Variables for the Tetrameric Model Used to Determine the Quaternary Structure of the Human Muscarinic Receptor, M_2R, Using Temporal and Spectral Resolution.

Experiment Type / Geometric Variables	Temporally Resolved	Spectrally Resolved
Ep	0.448	0.382
R1/R2	0.945	0.918
Alpha(°)	66.1	65.4
Residual	24.9	21.0

Using the geometric variables from the best fits, the length of each side of the parallelogram and the diagonal distances were calculated. The pairwise FRET efficiency E_p is dependent on the distance between the donor and the acceptor R_1, and was calculated using equation 1.

$$r_1 = R_0 \left(\frac{1-E_p}{E_p}\right)^{\frac{1}{6}} \quad (6)$$

r_2 was determined using the ratio of r_1/r_2, r_2. The diagonal lengths of the parallelogram were found using equations 2 and 3.

$$r_{d1}^2 = r_1^2 + r_2^2 + 2r_1 r_2 \cos\alpha \quad (7)$$

$$r_{d2}^2 = r_1^2 + r_2^2 - 2r_1 r_2 \cos\alpha \quad (8)$$

r_1 is the distance between two protomers at which the pairwise FRET efficiency occurs and corresponds to the width of the parallelogram, r_2 is the length of the parallelogram, r_{d1} and r_{d2} are the diagonals of the parallelogram as shown in figure 4.4c.

Table 2 shows r_1 ranges from 59Å to 61.8Å and r_2 ranges from 62.5Å to 67.3 Å for the temporally resolved and spectrally resolved, respectively. The diagonal distances r_{d1} and r_{d2} range from 66.3 Å to 69.9 Å and 101.8 Å to 108.6 Å respectively.

Table 4.2. Calculated Distances for the Parallelogram Shaped Oligomer for the Human Muscarinic Receptor, M_2R, Using Temporal and Spectral Resolution.

Experiment Type / Distances (Å)	Temporally Resolved	Spectrally Resolved
R1	59.0	61.8
R2	62.5	67.3
RD1	66.3	69.9
RD2	101.8	108.6

Conformational changes in the quaternary structures of GPCRs during activation has been a heavily investigated topic of study in recent years. Traditionally, GPCR activity has been regarded as binary where the model is in equilibrium between inactive and active state. However, this is restrictive and does not account for more recent observations of different conformational substates that have different functional effects [108]. This phenomenon has been studied using a variety of fluorescence-based techniques [104] such as, atomic force microscopy [109], electron microscopy

[110] and X-ray crystallography [111]. Generally, substates refer to the tertiary structure conformational changes undergone by the GPCRs when they switch from inactive to active or vice versa in response to ligands, as explored by Paprocki et al [64]. The quaternary structure oscillates between multiple conformation substates quickly in the presence of ligand. This results in an increase in both r_1 and r_2 distances with the addition of ligand [64]. This study also found that quaternary substates can also exist in the absence of ligand. Due to a low energy barrier between stable states, the GPCRs may fluctuate between multiple states faster than the instrument can detect [64].

Both temporally and spectrally resolved experiments yielded metahistograms that were fit with a parallelogram shaped tetramer. After refinement, both fits improved with the addition of the fixed Gaussian. The addition of the fixed Gaussian was necessary for two different reasons. Firstly, the relaxation of the GPCR into two or more stable conformations may result in the two or more substates for the quaternary structure and hence two or more FRET efficiency values. Secondly, the peak may be due to presence of higher order oligomers such as hexamers, octamers, etc. While virtually all the additional peaks predicted for the higher order oligomers fall at FRET efficiency values below or above those of tetramers, one or two of them could fall within those limits.

These errors will be explored in the following chapter.

Chapter 5

DISCUSSION AND OUTLOOK

In a study by Trujillo et al [99], three configurations of cytoplasmic trimeric constructs containing Cerulean (D), Venus (A) and non-fluorescent Amber (N) were expressed in the cytoplasm of CHO cells in the ratios NDA, ADN, and ADA. Both FLIM (one and two lifetime fits) and tiFRET were implemented to compare the feasibility of the tiFRET method. The results obtained using both methods were then compared to spectrally resolved FRET experiments conducted on the same constructs [99]. That study found that tiFRET performed comparably to the FLIM using one lifetime fit as well as behaved as anticipated by the kinetic theory of FRET [97, 100] is evidenced by the notable increase in FRET efficiency from the NDA and ADN to ADA [99]. When the FRET efficiencies of the NDA and ADN constructs are known, the FRET efficiency of the ADA construct can be calculated [65]. The predicted FRET efficiency values of ADA were experimentally verified since the values and their predicted uncertainties were in agreement. In this study, the FRET efficiencies for the ADA showed a notable increase compared to the NDA and ADN constructs, as expected according to the kinetic theory of FRET [99, 100] although the experimental values were systematically lower likely due to photobleaching.

The tiFRET method was also compared to a study also conducted by the Raicu lab [112] that investigated the effect of photobleaching on the fluorescent proteins used in the aforementioned study. Comparison between the two methods demonstrated that the FRET efficiencies of the temporally resolved study was significantly lower than that of the spectrally resolved study that was conducted at a lower excitation power and illumination time [99]. At a higher excitation power and illumination time, the results were comparable. Also, at this higher

power and illumination time, photobleaching of the acceptors via FRET was shown to occur [112] suggesting that a similar issue occurred. Photobleaching of the acceptor molecules leads to an overall decrease in FRET efficiency and may be a contributing factor in the discrepancies between both sets of FRET efficiencies [99].

In the work described in this thesis, apparent FRET efficiency maps containing pixel level FRET efficiencies determined via tiFRET for oligomeric configurations of unknown size were successfully generated. From the apparent FRET efficiency maps, histograms containing statistically significant peaks were obtained and a metahistogram of the frequency of peaks vs. the apparent FRET efficiency was generated. Using the standard spectrally resolved experiment method, metahistograms were obtained. A parallelogram shaped tetramer model was successfully used to fit both the temporally resolved and spectrally resolved experiments. This demonstrates the viability of the tiFRET method in obtaining the orientation and size of an oligomer of previously unknown configuration.

The resulting FRET efficiencies from the temporally resolved experiments were significantly higher than the FRET efficiencies obtained in the spectrally resolved experiments, subsequently, the dimensions of the oligomers calculated using the temporally resolved experiments were systematically lower than the distances calculated using the spectrally resolved experiments. Possible reasons for this discrepancy include blocking of the donor signal during data acquisition, and direct excitation of the acceptor paired with contamination of the donor signal with acceptor signal. Since only the donor signal is collected, when the donor signal is blocked signal from oligomers with more donors can also be blocked, this leads to a shift in the apparent FRET efficiencies obtained to higher FRET efficiencies. Similarly, direct excitation of the acceptor paired with contamination of the acceptor signal also leads to higher FRET efficiencies

since, the shorter relaxation times from the directly excited acceptor gives higher apparent FRET efficiencies.

Firstly for the temporally resolved experiments using M_2R, a 480±40nm filter was used in the excitation channel to select for the donor emission only. This filter has >90% transmission between the wavelengths 460-500 nm [113]. Fluorescent protein GFP_2 has a peak emission signal at approximately 506nm with approximately 90% emission at 500nm and 0% emission at 460nm [114] which suggests that the filter blocks an appreciable amount of donor signal as demonstrated in figure 5.1.. Secondly, since the emission peak of GFP_2 occurs at 509nm [115] and the excitation peak of YFP occurs at 531nm [116] and the 480/40nm bandwidth filter ranges from 440-520, acceptor contamination of the donor signal is inevitable. If the signal from direct excitation of the acceptor contaminates the donor signal, this leads to an increase in the FRET efficiencies calculated. If the shorter decay times from direct excitation of the acceptor are obtained and used as donor signal, this then shortens the fluorescence decay curves, resulting in a smaller integral of the fluorescence decay curves, overall leading to higher apparent FRET efficiencies. This likely contributes to the observed discrepancy between the metahistograms determined from tiFRET spectrometry and spectrally resolved FRET spectrometry as implemented in this study.

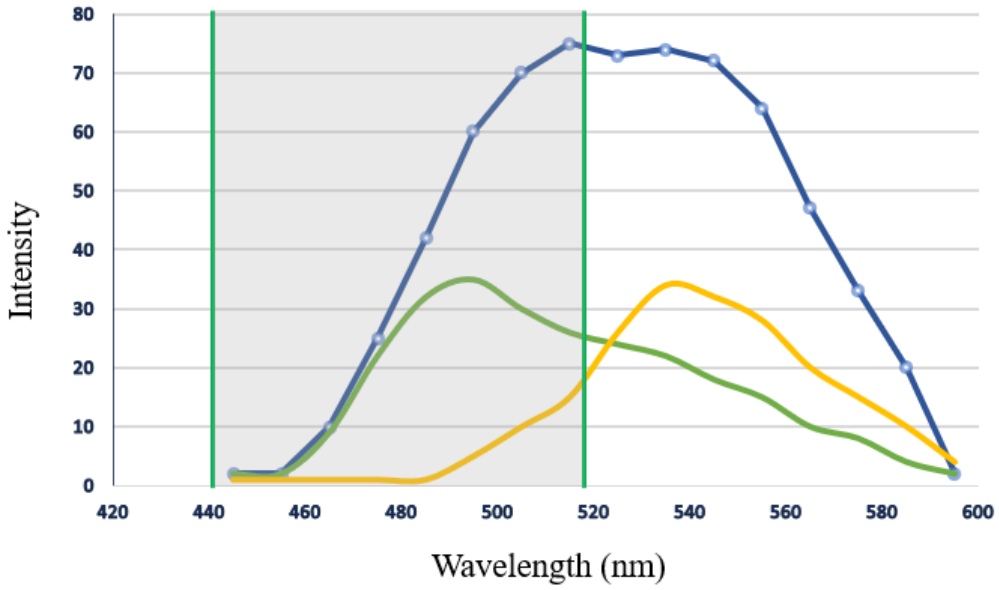

Figure 5.1. Schematic of a spectrum from an individual pixel with bandwidth filter overlayed. Each pixel in the spectrally resolved experiments contain a spectrum (blue) consisting of the donor (green) and acceptor (yellow) signal. The bandwidth filter used in the temporally resolved experiments restricts the detection of wavelengths emitted from the sample to a limited range (grey).

The tiFRET method can be used to perform FRET spectrometry experiments, despite the systematic difference in dimensions between the temporally resolved and spectrally resolved method. FRET spectrometry is often used to detect conformational changes in the GPCR oligomerization due to external changes in the environment, such as the effect of ligand on the binding of adaptor proteins such as β arrestin [117] or on oligomerization [64]. Since the purpose of the study would be to determine conformational differences between multiple states, the systematic effect would occur regardless, allowing the tiFRET method to be used.

In order to address the problem of the lack of acceptor signal, multi-wavelength time-resolved techniques can be applied, with which signals from different fluorophores may be detected and spectrally deconvoluted [118]. This can be achieved by placing a polychromator in

the detection path and a 16-channel multianode PMT with appropriate routes leading to data containing that are measured simultaneously at more than one spectral region [118]. By collecting the signal from the acceptor that has been directly excited, the FRET efficiency that is calculated accounts for the direct excitation of the acceptor. This should address the increase in FRET efficiency in the temporally resolved experiment versus the spectrally resolved experiments.

Another major difference between the image acquisition methods for the temporally resolved and spectrally resolved experiments, as outlined above is the use of the bandpass filters to collect the donor signal only for the temporally resolved. The current filter can let signal from the acceptor in the detection channel, which would artificially raise the FRET efficiency. Depending on the filters available, a different FRET pair may be a better option for this study.

Traditionally, the FRET efficiencies are sorted by protomer concentration. However, since the acceptor concentration could not be determined using the current data acquisition method, the FRET efficiencies were sorted using the donor concentration only. This can bias FRET efficiencies with higher acceptor signal. While this does not lead to the discrepancies in the current study since both spectral and temporal were sorted using donor only concentration, the overall efficacy of the study would benefit from multiwavelength FLIM, since the acceptors concentration can also be determined and the overall concentration of the system can be lowered.

References

1. Saba Rehman, N.R., Manjari Dimri, *Biochemistry, G Protein Coupled Receptors*. 2023: StatPearls Publishing LLC.
2. Bjarnadóttir, T.K., et al., *Comprehensive repertoire and phylogenetic analysis of the G protein-coupled receptors in human and mouse.* Genomics, 2006. **88**(3): p. 263-273.
3. Gacasan, S.B., D.L. Baker, and A.L. Parrill, *G protein-coupled receptors: the evolution of structural insight.* AIMS Biophys, 2017. **4**(3): p. 491-527.
4. Felder, C.C., et al., *Therapeutic opportunities for muscarinic receptors in the central nervous system.* Journal of Medicinal Chemistry, 2000. **43**(23): p. 4333-4353.
5. Kruse, A.C., et al., *Muscarinic acetylcholine receptors: novel opportunities for drug development.* Nature Reviews Drug Discovery, 2014. **13**(7): p. 549-560.
6. Haga, K., et al., *Structure of the human M2 muscarinic acetylcholine receptor bound to an antagonist.* Nature, 2012. **482**(7386): p. 547-51.
7. Ng, S.Y., L.T. Lee, and B.K. Chow, *Receptor oligomerization: from early evidence to current understanding in class B GPCRs.* Front Endocrinol (Lausanne), 2012. **3**: p. 175.
8. Marsango, S., et al., *Muscarinic receptor oligomerization.* Neuropharmacology, 2018. **136**(Pt C): p. 401-410.
9. Sun, P.D., C.E. Foster, and J.C. Boyington, *Overview of protein structural and functional folds.* Curr Protoc Protein Sci, 2004. **Chapter 17**(1): p. Unit 17 1.
10. Steward, K. *Essential Amino Acids: Chart, Abbreviations and Structure*. 2019 18 December 2023; Available from: https://www.technologynetworks.com/applied-sciences/articles/essential-amino-acids-chart-abbreviations-and-structure-324357.

11. Cornell, B. *Protein Structure*. 2016; Available from: https://old-ib.bioninja.com.au/higher-level/topic-7-nucleic-acids/73-translation/protein-structure.html.

12. Clare O'Connor, J.U.A., *Essentials of Cell Biology* 2010, Cambridge, MA: NPG Eduation.

13. Academy, K. *Introduction to Proteins and Amino Acids* Available from: www.khanacademy.org/science/biology/macromolecules/proteins-and-amino-acids/a/introduction-to-proteins-and-amino-acids.

14. Cooper, G., *The Cell: A Molecular Approach. 2nd Edition*. 2nd ed. 2000: Sinauer Associates Inc.

15. Boundless, *Lipid Molecule- Phospholipids*.

16. Hedin, L.E., K. Illergard, and A. Elofsson, *An introduction to membrane proteins.* J Proteome Res, 2011. **10**(8): p. 3324-31.

17. Cornell, B. *Membrane Proteins*. 2016; Available from: https://old-ib.bioninja.com.au/standard-level/topic-1-cell-biology/13-membrane-structure/membrane-proteins.html.

18. Zhao, J., et al., *G Protein-Coupled Receptors (GPCRs) in Alzheimer's Disease: A Focus on BACE1 Related GPCRs.* Front Aging Neurosci, 2016. **8**: p. 58.

19. Rosenbaum, D.M., S.G.F. Rasmussen, and B.K. Kobilka, *The structure and function of G-protein-coupled receptors.* Nature, 2009. **459**(7245): p. 356-363.

20. Harmar, A.J., *Family-B G-protein-coupled receptors.* Genome Biology, 2001. **2**(12).

21. Chaudhary, P.K. and S. Kim, *An Insight into GPCR and G-Proteins as Cancer Drivers.* Cells, 2021. **10**(12).

22. Yang, D.H., et al., *G protein-coupled receptors: structure- and function-based drug discovery.* Signal Transduction and Targeted Therapy, 2021. **6**(1).

23. Foster, S.R., et al., *Discovery of Human Signaling Systems: Pairing Peptides to G Protein-Coupled Receptors.* Cell, 2019. **179**(4): p. 895-+.

24. Cuffari, B. *What are Ligands?* September 2022; Available from: https://www.news-medical.net/life-sciences/Ligands-An-Overview.aspx.

25. Nussinov, R. and C.J. Tsai, *The Different Ways through Which Specificity Works in Orthosteric and Allosteric Drugs.* Current Pharmaceutical Design, 2012. **18**(9): p. 1311-1316.

26. Tuteja, N., *Signaling through G protein coupled receptors.* Plant Signal Behav, 2009. **4**(10): p. 942-7.

27. Negus, S.S., *Some implications of receptor theory for in vivo assessment of agonists, antagonists and inverse agonists.* Biochemical Pharmacology, 2006. **71**(12): p. 1663-1670.

28. Wacker, D., R.C. Stevens, and B.L. Roth, *How Ligands Illuminate GPCR Molecular Pharmacology.* Cell, 2017. **170**(3): p. 414-427.

29. Wess, J., *Muscarinic acetylcholine receptor knockout mice: Novel phenotypes and clinical implications.* Annual Review of Pharmacology and Toxicology, 2004. **44**: p. 423-450.

30. Gomeza, J., et al., *Pronounced pharmacologic deficits in M2 muscarinic acetylcholine receptor knockout mice.* Proceedings of the National Academy of Sciences of the United States of America, 1999. **96**(4): p. 1692-1697.

31. Ichlyama, S., et al., *The structure of the third intracellular loop of the muscarinic acetylcholine receptor M subtype.* Febs Letters, 2006. **580**(1): p. 23-26.

32. Gotte, G. and M. Menegazzi, *Protein Oligomerization.* Int J Mol Sci, 2023. **24**(13).

33. Marianayagam, N.J., M. Sunde, and J.M. Matthews, *The power of two: protein dimerization in biology.* Trends in Biochemical Sciences, 2004. **29**(11): p. 618-625.

34. Hashimoto, K. and A.R. Panchenko, *Mechanisms of protein oligomerization, the critical role of insertions and deletions in maintaining different oligomeric states.* Proceedings of the National Academy of Sciences of the United States of America, 2010. **107**(47): p. 20352-20357.

35. Changeux, J.P. and S.J. Edelstein, *Allosteric mechanisms of signal transduction.* Science, 2005. **308**(5727): p. 1424-1428.

36. Maggio, R., et al., *The impact of G-protein-coupled receptor hetero-oligomerization on function and pharmacology.* Febs Journal, 2005. **272**(12): p. 2939-2946.

37. Limbird, L.E. and R.J. Lefkowitz, *Negative cooperativity among beta-adrenergic receptors in frog erythrocyte membranes.* J Biol Chem, 1976. **251**(16): p. 5007-14.

38. Shimomura, O., F.H. Johnson, and Y. Saiga, *Extraction, purification and properties of aequorin, a bioluminescent protein from the luminous hydromedusan, Aequorea.* J Cell Comp Physiol, 1962. **59**: p. 223-39.

39. Prasher, D.C., et al., *Primary structure of the Aequorea victoria green-fluorescent protein.* Gene, 1992. **111**(2): p. 229-33.

40. Chalfie, M., et al., *Green fluorescent protein as a marker for gene expression.* Science, 1994. **263**(5148): p. 802-5.

41. Tsien, R.Y., *The green fluorescent protein.* Annu Rev Biochem, 1998. **67**: p. 509-44.

42. Zimmer, M., *GFP: from jellyfish to the Nobel prize and beyond.* Chemical Society Reviews, 2009. **38**(10): p. 2823-2832.

43. Gert-Jan Kremers, S.G.G., Paula J. Cranfill, Michael W. Davidson, David W. Piston, *Fluorescent Proteins at a glance.* Journal of Cell Science, 2011. **124**(2): p. 157-160.

44. Zimmer, M., *Green fluorescent protein (GFP): Applications, structure, and related photophysical behavior.* Chemical Reviews, 2002. **102**(3): p. 759-781.

45. David Piston, G.H.P., Jennifer Lippincott-Schwartz, Nathan S. Claxton and Michael W. Davidson. *Introduction to Fluorescent Proteins*. 09 March 2024]; Available from: https://www.microscopyu.com/techniques/fluorescence/introduction-to-fluorescent-proteins.

46. Sanderson, M.J., et al., *Fluorescence microscopy.* Cold Spring Harb Protoc, 2014. **2014**(10): p. pdb top071795.

47. Ishikawa-Ankerhold, H.C., R. Ankerhold, and G.P.C. Drummen, *Advanced Fluorescence Microscopy Techniques-FRAP, FLIP, FLAP, FRET and FLIM.* Molecules, 2012. **17**(4): p. 4047-4132.

48. Thomson, N.H., et al., *Protein tracking and detection of protein motion using atomic force microscopy.* Biophys J, 1996. **70**(5): p. 2421-31.

49. Dunn, K.W., M.M. Kamocka, and J.H. McDonald, *A practical guide to evaluating colocalization in biological microscopy.* American Journal of Physiology-Cell Physiology, 2011. **300**(4): p. C723-C742.

50. Tsekouras, K., et al., *A novel method to accurately locate and count large numbers of steps by photobleaching.* Molecular Biology of the Cell, 2016. **27**(22): p. 3601-3615.

51. Pincet, F., et al., *FRAP to Characterize Molecular Diffusion and Interaction in Various Membrane Environments.* Plos One, 2016. **11**(7).

52. Sekar, R.B. and A. Periasamy, *Fluorescence resonance energy transfer (FRET) microscopy imaging of live cell protein localizations.* Journal of Cell Biology, 2003. **160**(5): p. 629-633.

53. Stoneman, M.R. and V. Raicu, *Fluorescence-Based Detection of Proteins and Their Interactions in Live Cells.* Journal of Physical Chemistry B, 2023. **127**(21): p. 4708-4721.

54. Kural, C., H. Balci, and P.R. Selvin, *Molecular motors one at a time: FIONA to the rescue.* Journal of Physics-Condensed Matter, 2005. **17**(47): p. S3979-S3995.

55. Axelrod, D., et al., *Mobility measurement by analysis of fluorescence photobleaching recovery kinetics.* Biophys J, 1976. **16**(9): p. 1055-69.

56. Wüstner, D., et al., *Quantitative fluorescence loss in photobleaching for analysis of protein transport and aggregation.* Bmc Bioinformatics, 2012. **13**.

57. Bajar, B.T., et al., *A Guide to Fluorescent Protein FRET Pairs.* Sensors, 2016. **16**(9).

58. Zimmermann, T., et al., *Spectral imaging and linear un-mixing enables improved FRET efficiency with a novel GFP2-YFP FRET pair.* FEBS Lett, 2002. **531**(2): p. 245-9.

59. Stryer, L. and R.P. Haugland, *Energy transfer: a spectroscopic ruler.* Proc Natl Acad Sci U S A, 1967. **58**(2): p. 719-26.

60. Algar, W.R., *Key Steps to Follow in a FRET Experiment.* Spectroscopy, 2022. **37**(8): p. 46-50.

61. Masharina, A., et al., *A Fluorescent Sensor for GABA and Synthetic GABA Receptor Ligands.* Journal of the American Chemical Society, 2012. **134**(46): p. 19026-19034.

62. European Society of Animal Cell Technology General, M., et al., *Animal Cell Technology: From Target to Market : Proceedings of the 17th ESACT Meeting Tylösand, Sweden, June 10–14, 2001*. 1st 2001. ed. ESACT Proceedings 1. 2001, Dordrecht: Springer Netherlands : Imprint: Springer.

63. Adhikari, D.P., et al., *Comparative photophysical properties of some widely used fluorescent proteins under two-photon excitation conditions.* Spectrochimica Acta Part a-Molecular and Biomolecular Spectroscopy, 2021. **262**.

64. Paprocki, J., et al., *In-Cell Detection of Conformational Substates of a G Protein-Coupled Receptor Quaternary Structure: Modulation of Substate Probability by Cognate Ligand Binding.* J Phys Chem B, 2020. **124**(45): p. 10062-10076.

65. Patowary, S., et al., *Experimental Verification of the Kinetic Theory of FRET Using Optical Microspectroscopy and Obligate Oligomers.* Biophysical Journal, 2015. **108**(7): p. 1613-1622.

66. Becker, W., *Fluorescence lifetime imaging - techniques and applications.* Journal of Microscopy, 2012. **247**(2): p. 119-136.

67. Datta, R., et al., *Fluorescence lifetime imaging microscopy: fundamentals and advances in instrumentation, analysis, and applications.* Journal of Biomedical Optics, 2020. **25**(7).

68. Constantin Kappel, L.K., James DeRose. *What is FRET with FLIM (FLIM-FRET)?* 2022; Available from: https://www.leica-microsystems.com/science-lab/life-science/what-is-fret-with-flim/.

69. Guo, H., et al., *Methods used to study the oligomeric structure of G-protein-coupled receptors.* Biosci Rep, 2017. **37**(2).

70. McKenzie, D.M., et al., *Utility of FRET in studies of membrane protein oligomerization: The concept of the effective dissociation constant.* Biophys J, 2023. **122**(20): p. 4113-4120.

71. King, C., et al., *Fully quantified spectral imaging reveals in vivo membrane protein interactions.* Integr Biol (Camb), 2016. **8**(2): p. 216-29.

72. Raicu, V. and D.R. Singh, *FRET spectrometry: a new tool for the determination of protein quaternary structure in living cells.* Biophys J, 2013. **105**(9): p. 1937-45.

73. Raicu, V., et al., *Protein interaction quantified by spectrally resolved fluorescence resonance energy transfer.* Biochemical Journal, 2005. **385**: p. 265-277.

74. Singh, D.R., et al., *Determination of the quaternary structure of a bacterial ATP-binding cassette (ABC) transporter in living cells.* Integr Biol (Camb), 2013. **5**(2): p. 312-23.

75. AbdAlla, S., et al., *Increased AT(1) receptor heterodimers in preeclampsia mediate enhanced angiotensin II responsiveness.* Nat Med, 2001. **7**(9): p. 1003-9.

76. Biebermann, H., et al., *Autosomal-dominant mode of inheritance of a melanocortin-4 receptor mutation in a patient with severe early-onset obesity is due to a dominant-negative effect caused by receptor dimerization.* Diabetes, 2003. **52**(12): p. 2984-2988.

77. Mishra, A.K., et al., *Quaternary structures of opsin in live cells revealed by FRET spectrometry.* Biochemical Journal, 2016. **473**: p. 3819-3836.

78. Maggio, R., Z. Vogel, and J. Wess, *Coexpression Studies with Mutant Muscarinic Adrenergic-Receptors Provide Evidence for Intermolecular Cross-Talk between G-Protein-Linked Receptors.* Proceedings of the National Academy of Sciences of the United States of America, 1993. **90**(7): p. 3103-3107.

79. Cottet, M., et al., *BRET and Time-resolved FRET strategy to study GPCR oligomerization: from cell lines toward native tissues.* Front Endocrinol (Lausanne), 2012. **3**: p. 92.

80. Asher, W.B., et al., *Single-molecule FRET imaging of GPCR dimers in living cells.* Nature Methods, 2021. **18**(4): p. 397-+.

81. McMillin, S.M., et al., *Structural Basis of M Muscarinic Receptor Dimer/Oligomer Formation.* Journal of Biological Chemistry, 2011. **286**(32): p. 28584-28598.

82. Goin, J.C. and N.M. Nathanson, *Quantitative analysis of muscarinic acetylcholine receptor homo- and heterodimerization in live cells: regulation of receptor down-regulation by heterodimerization.* J Biol Chem, 2006. **281**(9): p. 5416-25.

83. Patowary, S., et al., *The muscarinic M2 acetylcholine receptor exists as two differently Sized complexes at the plasma membrane.* Biochemical Journal, 2013. **452**: p. 303-312.

84. Pisterzi, L.F., et al., *Oligomeric Size of the M2 Muscarinic Receptor in Live Cells as Determined by Quantitative Fluorescence Resonance Energy Transfer.* Journal of Biological Chemistry, 2010. **285**(22): p. 16723-16738.

85. LeBert, D.C., et al., *Second harmonic generation microscopy in zebrafish.* Methods Cell Biol, 2016. **133**: p. 55-68.

86. Chanoca, A., et al., *Using fluorescence lifetime microscopy to study the subcellular localization of anthocyanins.* Plant J, 2016. **88**(5): p. 895-903.

87. Chacko, J.V. and K.W. Eliceiri, *Autofluorescence lifetime imaging of cellular metabolism: Sensitivity toward cell density, pH, intracellular, and intercellular heterogeneity.* Cytometry A, 2019. **95**(1): p. 56-69.

88. *WiscScan*. 11 March 2024]; Available from: https://loci.wisc.edu/wiscscan/.

89. *OpenScan*. 11 March 2024]; Available from: loci.wisc.edu/openscan.

90. *Small Business Collaboratory*. 11 March 2024]; Available from: uwm.edu/microspectroscopy-collaboratory/optimis-facility.

91. Stoneman, M.R., et al., *A general method to quantify ligand-driven oligomerization from fluorescence-based images.* Nat Methods, 2019. **16**(6): p. 493-496.

92. Biener, G., et al., *Development and experimental testing of an optical micro-spectroscopic technique incorporating true line-scan excitation.* Int J Mol Sci, 2013. **15**(1): p. 261-76.

93. *SPCImage Next Generation FLIM Data Analysis Software*. 2022, Becker & Hickl GmbH: Berlin, Germany.

94. Raicu, V., et al., *Determination of supramolecular structure and spatial distribution of protein complexes in living cells.* Nature Photonics, 2009. **3**(2): p. 107-113.

95. Stoneman, M.R., et al., *Fluorescence-based Methods for the Study of Protein-Protein Interactions Modulated by Ligand Binding.* Current Pharmaceutical Design, 2020. **26**(44): p. 5668-5683.

96. Paprocki, J.D., *Investigation of G Protein-Coupled Receptor Quaternary Structure Through Fluorescence Micro-Spectroscopy and Theoretical Modeling: Interdependence Between Receptor-Receptor and Receptor-Ligand Interactions*, in *Physics Department*. 2021, University of Wisconsin, Milwaukee: University of Wiscosin, Milwaukee.

97. Raicu, V., *Efficiency of resonance energy transfer in homo-oligomeric complexes of proteins.* J Biol Phys, 2007. **33**(2): p. 109-27.

98. Margineanu, A., et al., *Screening for protein-protein interactions using Forster resonance energy transfer (FRET) and fluorescence lifetime imaging microscopy (FLIM) (vol 6, 28186, 2016).* Scientific Reports, 2016. **6**.

99. Justin A. Trujillo, A.S.K., Dhruba P. Adhikari, Michael R. Stoneman, Jenu V. Chacko, Kevin W. Eliceiri, Valerica Raicu, *Implementation of FRET spectrometry using temporally re-solved fluorescence: A feasibility study*, I.J.o.M. Sciences, Editor. 2024: MDPI.

100. Raicu, V., *Ab Initio Derivation of the FRET Equations Resolves Old Puzzles and Suggests Measurement Strategies.* Biophysical Journal, 2019. **116**(7): p. 1313-1327.

101. Lippincott-Schwartz, J. and G.H. Patterson, *Development and use of fluorescent protein markers in living cells.* Science, 2003. **300**(5616): p. 87-91.

102. Stoneman, M.R., et al., *Quantifying the efficiency of various FRET constructs using OptiMiS™.* Biotechniques, 2012. **52**(3): p. 191-+.

103. Stoneman, M.R., et al., *Quaternary structure of the yeast pheromone receptor Ste2 in living cells.* Biochimica Et Biophysica Acta-Biomembranes, 2017. **1859**(9): p. 1456-1464.

104. Kobilka, B.K. and X. Deupi, *Conformational complexity of G-protein-coupled receptors.* Trends Pharmacol Sci, 2007. **28**(8): p. 397-406.

105. Swaminath, G., et al., *Probing the β adrenoceptor binding site with catechol reveals differences in binding and activation by agonists and partial agonists.* Journal of Biological Chemistry, 2005. **280**(23): p. 22165-22171.

106. Ye, L.B., et al., *Activation of the A adenosine G-protein-coupled receptor by conformational selection.* Nature, 2016. **533**(7602): p. 265-+.

107. Miao, Y.L. and J.A. McCammon, *Graded activation and free energy landscapes of a muscarinic G-protein-coupled receptor.* Proceedings of the National Academy of Sciences of the United States of America, 2016. **113**(43): p. 12162-12167.

108. Park, P.S., *Ensemble of G protein-coupled receptor active states.* Curr Med Chem, 2012. **19**(8): p. 1146-54.

109. Senapati, S., et al., *Differentiating between Inactive and Active States of Rhodopsin by Atomic Force Microscopy in Native Membranes.* Analytical Chemistry, 2019. **91**(11): p. 7226-7235.

110. Ruprecht, J.J., et al., *Electron crystallography reveals the structure of metarhodopsin I.* EMBO J, 2004. **23**(18): p. 3609-20.

111. Rasmussen, S.G., et al., *Crystal structure of the beta2 adrenergic receptor-Gs protein complex.* Nature, 2011. **477**(7366): p. 549-55.

112. Dhruba P. Adhikari, M.R.S., Gabriel Biener, Valerica Raicu, *Impact of photobleaching of fluorescent proteins on FRET measurements under two-photon excitation conditions*. 2024.

113. *480/40 nm BrightLine® single-band bandpass filter* Available from: https://www.idex-hs.com/store/product-detail/ff01_480_40_25/fl-001626.

114. *TagGFP2*. Available from: https://www.fpbase.org/protein/taggfp2/.

115. Mahon, M.J., *pHluorin2: an enhanced, ratiometric, pH-sensitive green florescent protein.* Adv Biosci Biotechnol, 2011. **2**(3): p. 132-137.

116. Chen, Y.L., et al., *Research Progresses and Applications of Fluorescent Protein Antibodies: A Review Focusing on Nanobodies.* Int J Mol Sci, 2023. **24**(5).

117. Jean-Charles, P.Y., S. Kaur, and S.K. Shenoy, *G Protein-Coupled Receptor Signaling Through beta-Arrestin-Dependent Mechanisms.* J Cardiovasc Pharmacol, 2017. **70**(3): p. 142-158.

118. Strat, D., et al., *Spectrally resolved fluorescence lifetime imaging microscopy: Forster resonant energy transfer global analysis with a one- and two-exponential donor model.* Journal of Biomedical Optics, 2011. **16**(2).